Photobodies enable the phase-separation and counterbalance of opposing phytochrome B actions in PIF5 degradation and stabilization

Ruth Jean Ae Kim[1,3], De Fan[1,3], Jiangman He[1,3], Keunhwa Kim[1,2], Juan Du[1], Meng Chen[1,*]

[1] Department of Botany and Plant Sciences, Institute for Integrative Genome Biology, University of California, Riverside, CA 92521, USA

[2] Current address: Plant Molecular Biology and Biotechnology Research Center, Gyeongsang National University, Jinju 52828, Republic of Korea

[2] These authors contributed equally.

* Address correspondence to meng.chen@ucr.edu.

ABSTRACT

Photoactivation of the plant photoreceptor and thermosensor phytochrome B (PHYB) triggers its condensation into subnuclear photobodies (PBs). However, the function of PBs remains frustratingly elusive. Here, we show that PHYB condensation enables the co-occurrence and competition of two antagonistic phase-separated signaling actions. We found that PHYB recruits PHYTOCHROME-INTERACTING FACTOR5 (PIF5) to PBs and, surprisingly, that PHYB exerts opposing roles in degrading and stabilizing PIF5. Perturbing PB size by overproducing PHYB provoked a biphasic PIF5 response: while a moderate increase in PHYB enhanced PIF5 degradation, further elevating the PHYB level stabilized PIF5 by retaining more of it in enlarged PBs. Our results support a model in which PHYB condensation stabilizes PIF5 in PBs to counteract PIF5 degradation in the surrounding nucleoplasm, thereby enabling an environmentally sensitive counterbalancing mechanism to titrate nucleoplasmic PIF5 and its transcriptional output. This PB-enabled signaling mechanism provides a framework for regulating a plethora of PHYB-interacting signaling molecules in diverse plant environmental responses. We propose that this function of PBs represents a general function of biomolecular condensates to allow distinct variations of a cellular process or signaling pathway to coexist and interact to generate dynamically adjustable integrated outputs within a single subcellular space.

INTRODUCTION

A universal architectural hallmark of the cell nucleus is various functionally distinct membraneless subnuclear organelles, collectively referred to as nuclear bodies[1–3]. Nuclear bodies act as liquid- or gel-like biomolecular condensates that are commonly thought to be excluded from the surrounding nucleoplasm via concentration-dependent, energetically favorable liquid-liquid phase separation (LLPS)[3–5]. Many nuclear bodies, such as nucleoli, Cajal bodies, nuclear speckles, paraspeckles, histone locus bodies, and promyelocytic leukemia protein (PML) bodies, are well characterized, and they are associated with diverse basic nuclear functions in transcription, splicing, replication, and DNA repair; therefore, nuclear bodies have broad implications for human diseases[1–3]. Accumulating observations have also documented the nonuniform subnuclear distribution of cell signaling molecules to nuclear bodies, in addition to the surrounding nucleoplasm. For instance, the tumor suppressor p53 is recruited to PML bodies[6,7]. However, the functional significance of the spatial segregation of signaling molecules into two phase-separated compartments—nuclear bodies and the surrounding nucleoplasm—remains elusive. A better understanding of the function of nuclear bodies in cell signaling requires new genetically tractable models connecting nuclear body dynamics to cell signaling. Photobodies (PBs) are plant nuclear bodies defined molecularly by the presence of the photoreceptor and thermosensor phytochrome B (PHYB)[8–11]. The environment controls PHYB activity and directly regulates both the assembly/dissolution of PBs and PHYB signaling. As such, PBs provide a unique experimental paradigm for interrogating the general principles of nuclear bodies in cell signaling.

PHYs are evolutionarily conserved red (R) and far-red (FR) photoreceptors in plants[12]. The prototypical plant PHY is a homodimer; each monomer contains an N-terminal photosensory module and a C-terminal output module[12,13]. PHYs can be photoconverted between

two relatively stable forms: the R-light-absorbing inactive Pr form and the FR-light-absorbing active Pfr form[12,13]. The genome of the reference plant species *Arabidopsis thaliana* (*Arabidopsis*) encodes five PHYs, PHYA-E, among which PHYB plays a prominent role[14]. The photoconversion of PHYB—both its photoactivation by R light and its photoinactivation by FR light—alters the Pfr/Pr equilibrium and the cellular concentration of the active PfrPfr homodimer, allowing plants to monitor changes in light quality, quantity, and periodicity. The amount of active PHYB can also be modulated by ambient temperature through temperature-dependent thermal reversion from Pfr to Pr[15], making PHYB a prominent thermosensor in addition to a photoreceptor[16,17]. By controlling the amount of active PHYB, environmental light and temperature cues regulate all aspects of plant development and growth, including germination, seedling establishment, shade avoidance, floral induction, senescence, and immunity[18,19]. PHYB signaling is best studied during *Arabidopsis* seedling establishment, where the perception of environmental cues by PHYB in the epidermal cells of the embryonic leaves (cotyledons) controls the biosynthesis of the mobile growth hormone auxin to regulate seedling morphogenesis, including promoting cotyledon expansion locally, as well as inhibiting the elongation of the embryonic stem (hypocotyl) remotely[18,19].

The PHYB-containing subnuclear organelle was named the "photobody" by Joanne Chory in reference to its dynamic assembly and dissolution in response to light[20]. The regulation of PBs by light and temperature has been extensively studied in *Arabidopsis* pavement epidermal cells using fluorescent-protein-tagged PHYB (PHYB-FP). The current model posits that PB formation and maintenance are driven by the condensation of the active PfrPfr form of PHYB. This conclusion is supported by several lines of evidence. First, PB formation and dissolution can be induced by the activation and inactivation of PHYB, respectively. Akira Nagatani, Ferenc

Nagy, and Eberhard Schäfer first reported that the photoactivation of green-fluorescent-protein-tagged PHYB (PHYB-GFP) triggers its nuclear accumulation and further compartmentalization into discrete subnuclear speckles, or PBs[21,22]. Conversely, during the light-to-dark transition or upon an FR treatment where PHYB reverts to the inactive form, PHYB-FP moves from PBs into the nucleoplasm[23–26]. Second, the steady-state pattern of PBs, particularly PB size, correlates with the amount of active PHYB[27]. Under intense R light (e.g., 10 μmol m^{-2} s^{-1}), where each PHYB molecule stays in the Pfr form at least 50% of the time, PHYB-FP assembles into two to ten large PBs of 0.7-2 μm in diameter[23,27–29]. In contrast, under dim R light, where PHYB stays as the Pr most of the time, PHYB-FP localizes to tens of small PBs of less than 0.1-0.7 μm in diameter, or it is dispersed evenly in the nucleoplasm[23,27,29]. Consistent with these observations, a constitutively active *phyB* mutant YHB, which carries a Y276H mutation in PHYB's chromophore attachment domain and locks PHYB in an active form, localizes to a few large PBs even in the dark[30]. In contrast, *phyB* mutants that destabilize the Pfr form, including by removing the disordered N-terminal extension[15,31,32], promote PB dissolution[27,31–33]. Third, PB formation relies on the dimerization of PHYB's C-terminal module[32,34,35]. A D1040V mutation in this module, which disrupts PHYB dimerization, abolishes PHYB's ability to form PBs[36]. Fourth, PHYB can undergo light-dependent LLPS into biomolecular condensates in mammalian cells[37–39]. The intramolecular attributes of PHYB required for PB formation *in vivo*, e.g., the C-terminal module and N-terminal extension, are also essential for PHYB LLPS in this heterologous system[37], supporting the idea that PB formation *in vivo* may be propelled by the LLPS of active PHYB alone.

PHYB controls diverse developmental responses primarily by regulating a family of basic helix-loop-helix transcription factors called PHYTOCHROME-INTERACTING

FACTORs (PIFs)[19,40,41]. In general, PIFs are antagonists of PHYB signaling. For instance, the five prominent PIFs—PIF1, PIF3, PIF4, PIF5, and PIF7—collectively promote hypocotyl elongation[19,40,41]. A central mechanism of PHYB signaling is to promote the degradation of PIFs[40]. PIF1, PIF3, PIF4, and PIF5 are rapidly degraded during the dark-to-light transition in a PHYB-dependent manner[42–45]. PHYB binds directly to the prototypical PIF, PIF3, to promote its phosphorylation by PHOTOREGULATORY PROTEIN KINASEs (PPKs), its ubiquitylation by the **c**ullin3-**R**ING E3 ubiquitin **l**igases with LIGHT-RESPONSE BRIC-A-BRAC/TRAMTRACK/BROADs (LRBs) as the substrate recognition subunit ($CRL3^{LRB}$), and the cullin1 E3 with EIN3-BINDING F BOX PROTEINs (EBFs) as the substrate recognition subunit ($CRL1^{EBF}$), and subsequent proteasome-dependent degradation[46–48]. In addition to regulating PIFs via direct interaction, PHYB also promotes PIF degradation indirectly by inhibiting the factors that stabilize PIFs, such as the COP1 (CONSTITUTIVE PHOTOMORPHOGENIC 1) and SPA (SUPPRESSOR OF PHYTOCHROME A-105) complex, which constitutes the substrate recognition subunits of the $CRL4^{COP1/SPA}$ E3 ubiquitin ligases[49–52]. Interestingly, although PIF1, PIF3, PIF4, and PIF5 are subject to PHYB-mediated degradation, they exhibit different accumulation patterns. While PIF1 and PIF3 accumulate only in darkness and become undetectable in the light[36,53], PIF4 and PIF5 can accumulate to significant levels under prolonged light treatment[36,44,54,55]; this accumulation plays an essential role in the response to warm temperatures during the daytime[54,56]. However, the mechanism that stabilizes PIF4 and PIF5 in the light remains elusive.

PB formation correlates with PHYB-mediated light responses, such as the inhibition of hypocotyl growth; therefore, PBs are considered to be associated with PHYB signaling[8,9]. A large collection of *phyB* mutants that are defective in PB formation also show attenuated PHYB

signaling, indicating that PB formation correlates with PHYB signaling[27,30–34]. Recent proteomics studies have revealed that many PHYB signaling components reside in PBs; these components include COP1, SPAs, PPKs, and transcription factors linking light and photoperiodic signaling, including PIF4, TANDEM ZINC-FINGER-PLUS 3 (TZP), EARLY FLOWERING 3 (ELF3), EARLY FLOWERING 4 (ELF4), and LUX ARRHYTHMO (LUX)[25,57–59], lending further support to the functional role of PBs in PHYB signaling. The current data support the model that PBs play an important role in PIF3 degradation. During the dark-to-light transition, FP-tagged PIF3 localizes to PBs before its degradation[42,60]. Conversely, PIF3 reaccumulation during the light-to-dark transition correlates with the disappearance of PBs[23]. Forward genetic screens have identified three PB-deficient mutants, *hmr* (*hemera*)[53,61,62], *rcb* (*regulator of chloroplast biogenesis*)[63], and *ncp* (*nuclear control of pep activity*)[64], in which PHYB-FP fails to form large PBs and PIF3 degradation is blocked in the light. Moreover, overexpressing PHYB's C-terminal output module alone, which constitutively localizes to PBs, is sufficient to mediate PIF3 degradation even in darkness[36].

Despite the accumulating evidence associating PBs with PIF3 degradation, the precise function of PBs remains frustratingly elusive. We still cannot unequivocally conclude that PBs are the sites of PIF3 degradation, and it is still unknown whether PBs also regulate other PIFs. A major challenge in dissecting the function of nuclear bodies, in general, has been the difficulty uncoupling the functional output of nuclear bodies from the surrounding nucleoplasm. Because components can diffuse between the nuclear body compartment and the surrounding nucleoplasm, manipulating those components may disrupt both their nuclear body assembly and their associated functional outputs, but this type of correlation cannot necessarily assign the function exclusively to the nuclear body pool. The previous approach of using loss-of-function

mutants in PHYB or PHYB signaling was likely to disrupt PHYB signaling in both PBs and the surrounding nucleoplasm and therefore could not uncouple the two. Another hurdle in studying PIF3 degradation was the difficulty monitoring its PB localization: because PIF3 does not accumulate to a detectable level in the light, FP-tagged PIF3 can only be observed briefly during the dark-to-light transition[42,60].

To circumvent these obstacles to characterizing PBs, we implemented two major strategic changes in the current study. First, we adopted PIF5 as a model because PIF5 accumulates in the light and therefore could potentially allow us to visualize its localization to PBs in light-grown seedlings[44,55], though the PB localization of PIF5 had not been reported previously. Second, instead of disrupting PBs using loss-of-function mutants in PHYB or PHYB signaling, we perturbed the PB size by increasing PHYB abundance. We reasoned that if PB formation is driven by the LLPS of PHYB, LLPS occurs at a critical concentration, above which PHYB molecules phase separate. Thus, the overproduction of PHYB is expected to result only in the growth of PBs without changing the concentration of PHYB in either the PB or the surrounding nucleoplasmic compartments[4,65] and, therefore, may only enhance the signaling output from PBs while leaving the functional output of the nucleoplasmic PHYB unchanged or less affected. Here, we show that PHYB recruits PIF5 as a client to PBs and, surprisingly, that PHYB exerts two opposing functions in both degrading and stabilizing PIF5. Perturbing PB size by overproducing PHYB allowed us to reveal that PHYB condensation stabilizes PIF5 in PBs to counteract PIF5 degradation in the surrounding nucleoplasm, thereby enabling a counterbalancing mechanism to titrate nuclear PIF5 and its signaling outputs. This novel PHYB signaling mechanism provides a framework by which PBs regulate a plethora of PHYB-interacting signaling molecules to generate diverse adaptive environmental responses in plants.

RESULTS

Increasing PHYB production alters PB size and dynamics

Instead of interrogating the function of PBs in loss-of-function *phyB* or PHYB signaling mutants, we explored an alternative approach: perturbing PBs by increasing PHYB abundance. To that end, we collected *Arabidopsis* lines expressing various amounts of PHYB. We previously reported the *PBC* line, which overexpresses CFP-tagged PHYB (**P**HY**B**-**C**FP) in the *phyB-9* background[32]. *PBC* exhibits a short hypocotyl phenotype, as it overexpresses PHYB-CFP at a level 65-fold that of the endogenous PHYB (Fig. 1a-c)[32]. To create lines expressing intermediate levels of PHYB between *PBC* and Col-0, we generated new transgenic lines in the *phyB-9* background carrying *PHYB* genomic DNA with a *CFP* sequence inserted immediately before the *PHYB* stop codon; we named them *gPBC* (***g****enomic* ***P****HY****B****-****C****FP*) lines. Two single-insertion *gPBC* lines, *gPBC-25* and *gPBC-29*, were selected for further analysis. The steady-state levels of PHYB-CFP in *gPBC-25* and *gPBC-29* were about 7- and 40-fold that of the endogenous PHYB level in Col-0, respectively (Fig. 1a-c). Both *gPBC* lines rescued the long-hypocotyl phenotype of *phyB-9*, indicating that PHYB-CFP was functional (Fig. 1a,b). Consistent with the PHYB levels, the hypocotyl length of *gPBC-25* was in between that of Col-0 and *PBC*, whereas the hypocotyl length of *gPBC-29* was similar to that of *PBC* (Fig. 1a,b). With the two new *gPBC* lines, we had a panel of five lines—*phyB-9*, Col-0, *gPBC-25*, *gPBC-29*, and *PBC*—with PHYB levels ranging from zero to 65-fold that of the wild-type level (Fig. 1a-c).

To test whether increasing the PHYB level enhances the size of PBs, we measured the volumes of PHYB-CFP PBs in *gPBC-25*, *gPBC-29*, and *PBC*. Indeed, the PB size increased with increases in the PHYB-CFP level. *PBC* had the largest PBs, which were on average more than 5-fold larger than those in *gPBC-25*, and the average PB volume of *gPBC-29* was three times

larger than that of *gPBC-25* (Fig. 1d,e). The fraction of PHYB-CFP localized to PBs also increased with the PHYB-CFP level (Fig. 1f). We used fluorescence recovery after photobleaching (FRAP) to assess the exchange of PHYB-CFP molecules between PBs and the surrounding nucleoplasm. To our surprise, the PBs from *gPBC-25* and *PBC* exhibited significant differences in the dynamics of PHYB-CFP. The fluorescence recovery in *gPBC-25* was only 31%, suggesting that the majority of PHYB-CFP molecules were not mobile (Fig. 1g). The percentage of fluorescence recovery in *PBC* was further reduced to 20%, suggesting that increasing PHYB-CFP abundance in *PBC* decreased the mobile fraction of PHYB-CFP in PBs, likely due to a transition to a gel-like state (Fig. 1g). Consistent with this observation, PHYB-CFP in the PBs from *PBC* showed an increase in the fluorescence recovery time compared with *gPBC-25*, indicating a reduction in the diffusion rate of *PHYB-CFP* in *PBC*. Together, these results suggest that increasing PHYB abundance enhances PB size by recruiting a larger fraction of PHYB to the PB compartment and retaining PHYB for a longer time in PBs due to a transition to a gel-like state. Thus, this panel of lines with various PB sizes and PHYB-CFP dynamics provides a new opportunity to interrogate the function of PBs in PIF degradation.

PIF5 is a short-lived protein localized in PBs

To investigate the function of PBs in PIF regulation, we generated transgenic lines expressing PIF5 fused with Myc and mCherry to the N-terminus (mCherry-PIF5) under the native *PIF5* promoter in the null *pif5-3* mutant background. Two independent transgenic lines with a single insertion of the transgene, named *mCherry-PIF5/pif5-3 #8* and *#9*, were selected for further analysis. The *pif5-3* mutant exhibited a short hypocotyl phenotype at 16°C. Because PIF5 is required for the warm temperature-induced hypocotyl elongation, the defect of *pif5-3* in hypocotyl growth became more pronounced at 27°C (Fig. 2a,b)[44,54]. The *mCherry-PIF5/pif5-3*

lines rescued the hypocotyl growth defects of *pif5-3* at both temperatures (Fig. 2a,b), indicating that mCherry-PIF5 was functional. Similar to endogenous PIF5, mCherry-PIF5 accumulated in the light and could be detected by immunoblotting using anti-PIF5 antibodies (Fig. 2c). Despite being controlled by the native *PIF5* promoter, the steady-state levels of mCherry-PIF5 in the transgenic lines were higher than that of endogenous PIF5 in Col-0. The mCherry-PIF5 level in line *#8* was more than 5-fold that of line #9 and more than 10-fold that of endogenous PIF5 in Col-0 (Fig. 2c). However, to our surprise, no mCherry signal could be detected by confocal microscopy in either of the *mCherry-PIF5/pif5-3* transgenic lines. We reasoned that this discrepancy might be attributable to a faster turnover rate of mCherry-PIF5 compared to the maturation time of mCherry. Newly synthesized fluorescent proteins require maturation to become fluorescent. The reported maturation time of mCherry is more than 60 min[66]. Therefore, if the half-life of mCherry-PIF5 is significantly shorter than 60 min, the newly synthesized mCherry-PIF5 would have been degraded before becoming fluorescent. If this were the case, non-fluorescent mCherry-PIF5 should be detectable by immunolocalization. Indeed, Myc-tagged mCherry-PIF5 could be detected via immunofluorescence staining using anti-Myc antibodies. Interestingly, mCherry-PIF5 was localized to discrete punctate structures at both 16ºC and 27ºC (Fig. 2d). Simultaneously labeling PHYB using anti-PHYB antibodies demonstrated that mCherry-PIF5 colocalized with PHYB in PBs (Fig. 2d,e). Thus, these results indicate that mCherry-PIF5 is a short-lived protein that colocalizes with PHYB in PBs *in vivo*.

PHYB signaling both degrades and stabilizes PIF5

The fact that mCherry-PIF5 was short-lived in PBs might suggest that mCherry-PIF5 degradation occurs in PBs. However, it was equally possible that mCherry-PIF5 is degraded in

the nucleoplasm and that because mCherry-PIF5 is exchanged between the nucleoplasm and PBs, both the nucleoplasmic and PB pools of mCherry-PIF5 are short-lived. One way to distinguish between these two possibilities would be to test whether and how perturbing PBs alters PIF5 degradation. For example, if PIF5 is degraded in PBs, increasing the size of PBs should recruit more PIF5 to PBs for degradation and therefore would be expected to reduce the steady-state level of PIF5. We examined the endogenous levels of PIF5 in the panel of lines expressing various amounts of PHYB (Fig. 1a-c). To our surprise, PIF5 showed a biphasic response to increases in PHYB abundance. In the range of zero to low levels of PHYB in *phyB-9*, Col-0, and *gPBC-25*, the steady-state level of PIF5 decreased with the increases in PHYB (Fig. 3a-c), supporting the current model that PHYB promotes PIF5 degradation in the light. However, unexpectedly, further increasing PHYB abundance in *gPBC-29* and *PBC* enhanced PIF5 accumulation (Fig. 3a,b). Because the transcript levels of *PIF5* remained the same in *phyB-9*, Col-0, *gPBC-25*, *gPBC-29*, and *PBC* (Fig. 3c), the variations in PIF5 in these lines were due to either PIF5 biosynthesis or degradation. We next examined the degradation kinetics of PIF5 in Col-0, *gPBC-25*, and *PBC* by treating the cell lysates with the translation inhibitor cycloheximide and then monitoring the disappearance of PIF5 over time. These experiments showed that PIF5 was degraded at a much faster rate in *gPBC-25* than in Col-0, whereas PIF5 degradation was dramatically attenuated in *PBC* (Fig. 3d,e). Thus, the accumulation of PIF5 in *PBC* and *gPBC-29* was most likely due to the PHYB-mediated stabilization of PIF5. These results suggest that PHYB signaling exerts opposing roles in both degrading and stabilizing PIF5, the balance of which can be adjusted by altering the PHYB level. Because a major change from *gPBC-25* to *PBC* was an increase in the size of PBs (Fig. 1d), one possible explanation is that while PHYB degrades PIF5 in the nucleoplasm, it stabilizes PIF5 in PBs; as such, increasing

the PB size in *PBC* could recruit more PIF5 to PBs to switch the balance towards PIF5 stabilization.

PHYB recruits and stabilizes PIF5 in PBs

To further examine the role of PBs in stabilizing PIF5, we reasoned that if PIF5 were stabilized due to its enhanced recruitment to the enlarged PBs in *PBC*, we might be able to observe the accumulation of stabilized or longer-lived mCherry-PIF5 proteins in PBs in *PBC*. To that end, we generated transgenic lines expressing mCherry-PIF5 tagged with human influenza hemagglutinin (HA) (HA-mCherry-PIF5) under the constitutive *UBIQUITIN 10* promoter in *PBC* (*mCherry-PIF5/PBC*). We selected two *mCherry-PIF5/PBC* lines (*#1* and *#9*) for further analysis. The *mCherry-PIF5ox/PBC* lines were taller than *PBC* at both 16ºC and 27ºC, suggesting that the HA-tagged mCherry-PIF5 was functional (Fig. 4a,b). Both *mCherry-PIF5/PBC* lines accumulated more mCherry-PIF5 than endogenous PIF5 at 16ºC and 27ºC; the mCherry-PIF5 levels in *mCherry-PIF5ox/PBC #1* were more than 20-fold greater than that of the endogenous PIF5 in Col-0 (Fig. 4c). Interestingly, unlike the *mCherry-PIF5/pif5-3* lines, we could observe the fluorescent signal of mCherry-PIF5 in the *mCherry-PIF5ox/PBC* lines using confocal microscopy (Fig. 4d). Similar to the *mCherry-PIF5/pif5-3* lines, mCherry-PIF5 also colocalized with PHYB-CFP in PBs in the *mCherry-PIF5ox/PBC* lines at both 16ºC and 27ºC in the light (Fig. 4d,e). In dark-grown *mCherry-PIF5ox/PBC* seedlings where there were no PHYB-CFP PBs, mCherry-PIF5 was evenly dispersed in the nucleoplasm (Fig. 4f), implying that mCherry-PIF5 was recruited to PBs in the light by PHYB. The fact that mCherry-PIF5 became detectable by confocal microscopy suggests that the half-life of the mCherry-PIF5 in *mCherry-PIF5ox/PBC* was significantly longer than that of the mCherry-PIF5 in *mCherry-PIF5/pif5-3*.

Supporting this conclusion, the degradation kinetics of mCherry-PIF5 in *mCherry-PIF5ox/PBC* were slower than those in *mCherry-PIF5/pif5-3* (Fig. 4g,h). Together, these results support the model that PHYB recruits and stabilizes PIF5 in PBs and that the PIF5-stabilizing function of PHYB is enhanced in *PBC* by retaining more PIF5 in larger PBs.

Reducing PB size accelerates PIF5 degradation

One caveat of our experimental design was that the expression of mCherry-PIF5 in *mCherry-PIF5/PBC* was driven by the constitutive *UBIQUITIN10* promoter; as a result, the level of mCherry-PIF5 in *mCherry-PIF5/PBC* was higher than that in *mCherry-PIF5/pif5-3*. Therefore, there is a slight possibility that the discrepancy between the two lines was due to the higher level of mCherry-PIF5 in *mCherry-PIF5/PBC*. To eliminate this possibility, we tested whether PIF5 stability could be manipulated by altering the PBs in *mCherry-PIF5/PBC*. We reasoned that if recruiting PIF5 to PBs prevents PIF5 degradation in the surrounding nucleoplasm, reducing PB size in *mCherry-PIF5/PBC* under dimmer light should shift the balance of PHYB signaling from stabilizing PIF5 to degrading PIF5. To test this hypothesis, we compared the size and dynamics of PBs, as well as PIF5 degradation, in *mCherry-PIF5ox/PBC* #9 grown under 10 μmol m^{-2} s^{-1} or a dimmer 0.5 μmol m^{-2} s^{-1} R light. The *mCherry-PIF5ox/PBC* seedlings grown under 0.5 μmol m^{-2} s^{-1} R light were significantly taller than the *mCherry-PIF5ox/PBC* seedlings grown under 10 μmol m^{-2} s^{-1} and *PBC* seedlings grown 0.5 μmol m^{-2} s^{-1} R light (Fig. 5a,b), which suggests that mCherry-PIF5 in *mCherry-PIF5ox/PBC* was more abundant or active under the dim light. As expected, PHYB-CFP PBs became significantly smaller under the dim light (Fig. 5c,d). Interestingly, mCherry-PIF5 was detectable using confocal microscopy in only 75.3% of PBs (Fig. 5e), suggesting that mCherry-PIF5 might

be less stable. Supporting this conclusion, the steady-state levels of mCherry-PIF5 and endogenous PIF5 decreased dramatically in *mCherry-PIF5ox/PBC* under 0.5 μmol m^{-2} s^{-1} R light compared to 10 μmol m^{-2} s^{-1} R light (Fig. 5f). The dimmer light treatment also reduced the PIF5 level in *PBC*, indicating that the effects in *mCherry-PIF5ox/PBC* were not caused by the overexpression of mCherry-PIF5. Consistently, the degradation kinetics were dramatically increased in *mCherry-PIF5ox/PBC* under dim light conditions (Fig. 5g). PHYB-CFP became more dynamic in the small PBs under 0.5 μmol m^{-2} s^{-1} R light, suggesting that dimmer light promoted a gel-to-liquid transition (Fig. 5h). Intriguingly, the dynamics of mCherry-PIF5 stayed the same between high and low light conditions (Fig. 5i). Therefore, although the large and small PBs have different PIF5-binding capacities, their PIF5 binding affinities may be similar. Therefore, reducing the PB size promotes PIF5 degradation, likely by enhancing the nucleoplasmic partitioning of PIF5 and PHYB, which triggers PIF5 phosphorylation and degradation. Together, these results provide further evidence for our conclusion that recruiting PIF5 to PBs stabilizes PIF5 by preventing its degradation in the surrounding nucleoplasm.

DISCUSSION

Reports published more than 20 years ago described how light triggers the localization of photoactivated PHYB to discrete PBs, creating two spatially separated pools of PHYB—a concentrated pool in PBs and a dilute pool in the surrounding nucleoplasm—and that PB size depends on the amount of active PHYB and therefore could be directly regulated by light intensity and quality (i.e., the R/FR ratio)[21,22,27]. However, the functional significance of this spatial segregation of active PHYB remained frustratingly elusive. Here, using PIF5 as a model, we show that PHYB recruits PIF5 as a client to PBs and, surprisingly, that PHYB exerts two

opposing functions in both degrading and stabilizing PIF5. Different from previous studies on PBs, we perturbed PBs by increasing PHYB abundance. This approach allowed us to uncouple the function of PHYB in PBs from that of PHYB in the surrounding nucleoplasm. Our results support the model that the condensation of PHYB segregates the opposing signaling mechanisms of PIF5 stabilization and degradation into two subnuclear compartments: a PIF5-stabilizing environment in PBs and a PIF5-degrading environment in the surrounding nucleoplasm (Fig. 6). As such, environmentally controlled PB dynamics can regulate the PB-and-nucleoplasmic partitioning of PHYB and PIF5 to balance these two antagonistic signaling actions, thereby enabling an environmentally sensitive counterbalancing mechanism for titrating the nucleoplasmic concentration of PIF5 and its transcriptional output. Because the regulation of the stability of PHYB-associated signaling components is a major mechanism of light signaling[19,20,40], this novel PB-dependent counterbalancing mechanism provides the framework for regulating a plethora of PHYB-interacting signaling molecules in diverse plant environmental responses. We propose that this PB function represents a general function of biomolecular condensates to allow distinct variations of a cellular process or signaling pathway to coexist and interact to generate dynamically adjustable integrated outputs within a single subcellular space.

PHYB recruits and stabilizes PIF5 in PBs

Our results indicate that PHYB recruits PIF5 to PBs for PIF5 stabilization. We demonstrated for the first time that PIF5 localizes to PBs. This conclusion is supported by the colocalization of mCherry-PIF5 with endogenous PHYB in PBs in *mCherry-PIF5/pif5-3* and with PHYB-CFP PBs in *mCherry-PIF5ox/PBC* (Figs. 2d,e and 4d,e). We showed that the slow maturation time of FPs may pose a major obstacle in observing FP-tagged PIFs in live cells. The short-lived mCherry-PIF5 in the *mCherry-PIF5/pif5-3* lines could only be detected using

immunofluorescence staining, not via confocal microscopy (Fig. 2d). This technical hurdle might explain the surprisingly low number of detailed investigations into the subcellular localization of FP-tagged PIFs compared with the overwhelming number of reports on PIFs' functions. Although the lack of mCherry fluorescence hindered our ability to observe mCherry-PIF5 in live cells from the *mCherry-PIF5/pif5-3* lines, we serendipitously found that the absence and presence of mCherry fluorescence serves as an internal reporter for assessing the stability or half-life of mCherry-PIF5. When PIF5 degradation was attenuated in *mCherry-PIF5ox/PBC*, the fluorescence of mCherry-PIF5 became detectable using confocal microscopy, providing direct evidence demonstrating the retention of stabilized mCherry-PIF5 in PBs (Fig. 4d). Because the PB localization of mCherry-PIF5 in *mCherry-PIF5ox/PBC* occurred only in the light (Fig. 4d,f), these results support the idea that PIF5 is recruited to PBs by PHYB, likely via direct interaction[43]. This conclusion corroborates the results from a proteomics analysis showing that PBs comprise PHYB and primary and secondary PHYB-interacting proteins[25,57,58]. However, PIF5 was not identified in these proteomics experiments, which may be due to the timing and conditions used. One concept of biomolecular condensates is the concept of scaffolds and clients[67]. Scaffold molecules are considered the drivers of phase separation, whereas molecules that are recruited into biomolecular condensates formed by scaffolds are called clients[67]. Applying this concept to PBs, the current data suggest that PHYB is a scaffold component, whereas PIF5 is a client component recruited to PBs, likely via direct interactions with PHYB and other PB components (Fig. 6). Supporting this model, altering PB size by manipulating the concentration of active PHYB changed the dynamics of the scaffold (PHYB) but not of the client (PIF5) (Fig. 5h,i). Therefore, changes in PB size alter only PBs' capacity for PIF5 binding, not their affinity to this client. Together, our results reveal that in addition to promoting PIF5

degradation, PHYB signaling can also stabilize PIF5 by recruiting PIF5 to PBs, providing a mechanism that allows PIF5 to accumulate in the light.

Phase-separation of two opposing signaling actions

Our results support the model that PHYB condensation segregates the PIF5-stabilizing environment in PBs from the PIF5-degrading environment in the surrounding nucleoplasm (Fig. 6). PHYB-mediated degradation of PIFs has been invoked as the central mechanism of light signaling[19,40,41]. PIF5 is relatively stable in dark-grown seedlings and, upon exposure to light, PHYA and PHYB induce the rapid phosphorylation and degradation of PIF5[43,44]. Our results suggest that PHYB mediates PIF5 degradation in the nucleoplasm but not in PBs. This conclusion is supported by the following evidence. First, mCherry-PIF5 could accumulate in PBs in *mCherry-PIF5/pif5-3* and *mCherry-PIF5ox/PBC*; in particular, the accumulation of longer-lived mCherry-PIF5 in *mCherry-PIF5ox/PBC* clearly uncoupled PBs from the function of PHYB signaling in PIF5 degradation. Second, PB size correlated positively with PIF5 stabilization and negatively with PIF5 degradation. A transition from small PBs in *mCherry-PIF5/pif5-3* to large PBs in *mCherry-PIF5ox/PBC* switched the balance of PHYB signaling from degrading to stabilizing PIF5 (Figs. 2-4). Consistently, growing *mCherry-PIF5ox/PBC* seedlings in dimmer light, which induced the transition from large PBs to small PBs, accelerated PIF5 degradation (Fig. 5). These results support the conclusion that reducing the PB size or the capacity of PIF5 binding enhances PIF5 degradation in the nucleoplasm. The mechanism that distinguishes the PIF5-stabilizing environment in PBs and the PIF5-degrading environment in the surrounding nucleoplasm requires further investigation. Previous studies have suggested that PIF5 degradation is mediated by the $CRL4^{COP1/SPA}$ E3 ubiquitin ligase[55]. PHYB interacts directly with COP1 and SPAs via different domains: while the N-terminal photosensory module interacts with

COP1[68], the C-terminal output module confers a strong interaction with SPAs[49,50,69]. As such, PHYB inhibits the activity of $CRL4^{COP1/SPA}$ by blocking the COP1-SPA interaction[49–51,68,70]. Both COP1 and SPAs have been identified as PB components[25,59]; therefore, it is likely that the high concentration of PHYB in PBs facilitates the dissociation of COP1-SPA complexes (Fig. 6). In addition, cullin4 has been shown to disperse evenly in the nucleoplasm[71] and has not been identified as a PB constituent[25,59]. Therefore, the CRL4 core localizes only in the nucleoplasm but not in PBs, providing another mechanism explaining the distinct functions in PBs and the surrounding nucleoplasm (Fig. 6). In this model, the dynamic changes in PBs would also regulate the amount of functional $CRL4^{COP1/SPA}$ complex in the nucleoplasm.

The current data suggest that recruiting PIF5 to PBs sequesters it away, impeding its functions in promoting hypocotyl elongation. It was proposed previously that the PB localization of PIF7 sequesters it, inhibiting its transcriptional activator activities in the nucleoplasm[72]. Our results suggest that recruiting PIF5 to PBs may also attenuate its function in activating growth-relevant genes. Reducing the PB size in *mCherry-PIF5ox/PBC* in dimmer light, which should enhance the nucleoplasmic pool of PIF5, promoted hypocotyl elongation (Fig. 5a,b). However, counterintuitively, the levels of both endogenous PIF5 and mCherry-PIF5 in *mCherry-PIF5ox/PBC* were reduced in the dimmer light compared to the higher light condition (Fig. 5f), indicating that the steady-state level of PIF5 does not correlate with its function in promoting hypocotyl elongation. One possibility is that PIF5 degradation is associated or coupled with its transcription activation activity. A similar mechanism has been proposed for PIF3 because blocking PIF3 degradation in the *hmr* mutant also attenuates the activation of its target genes[62]. Together, the current data support the model that environmentally controlled PB dynamics can titrate nucleoplasmic PIF5 and its associated signaling outputs.

The function of PBs in stabilizing PIF5 may not be extrapolated to other PIFs because PIFs vary in their light-dependent accumulation patterns and degradation mechanisms. For example, unlike PIF5, PIF1 and PIF3 accumulate only in the dark, and they are below detectable levels via immunoblotting in the light. Therefore, it is unlikely that PBs play a role in stabilizing these two PIFs. The degradation of PIF1 is mediated by $CRL4^{COP1/SPA}$ and $CRL1^{CTG10}$ with the F-box protein COLD TEMPERATURE GERMINATION 10 (CTG10) as the substrate recognition subunit[69,73], whereas PIF3 is degraded by $CRL3^{LRB}$ and $CRL1^{EBF}$. PBs have been proposed to be required for PIF1 and PIF3 degradation. Similar to PIF5, PIF4 can also accumulate in the light. However, PIF4 is ubiquitylated by the cullin3-based E3 ligase using BLADE ON PETIOLE (BOP1/2) as the substrate recognition components[74]. When coexpressed with PHYB, FP-tagged PIF4, as well as PIF3 and PIF6/PIL2, localized with PHYB in biomolecular condensates in mammalian cells or protoplasts in a PHYB-dependent manner, supporting the idea that PHYB may be able to recruit PIF4 to PBs[37–39]. However, the PB localization of PIF4 in *Arabidopsis* has not been carefully studied, and the potential role of PBs in stabilizing PIF4 in the light remains to be experimentally verified.

Perturbing PBs by modulating the PHYB level

A major difference that distinguishes this study from the previous investigations about PBs is the approach used to perturb PBs. Because components can diffuse between membraneless organelles and the surrounding environment, a major challenge in studying the function of nuclear bodies has been the difficulty in dissecting the functional role of components in nuclear bodies vs the surrounding nucleoplasm. Conventional approaches using loss-of-function mutants of nuclear body components may yield a correlation between assembly and a functional output; however, such a correlation is usually not sufficient to discern the function of

nuclear bodies from functions in the surrounding nucleoplasm. Here, we perturbed the PB size by increasing PHYB abundance. If PB formation is driven by the LLPS of PHYB, increasing the PHYB level is expected to only enlarge the PB size without changing the concentrations of PHYB in the nucleoplasm and therefore may specifically enhance the functional output within PBs[4,65]. Consistent with the hypothesis, increasing PHYB abundance enlarged the PB size (Fig. 1d,e). The majority of PHYB-CFP in PBs was immobile in *gPBC-25* (Fig. 1g); this attribute of PHYB condensates was similar to the biomolecular condensates formed by PHYB alone in mammalian cells[37], suggesting that PHYB molecules were tightly bound in PBs. Surprisingly, however, further increasing the PHYB level in *PBC* dramatically reduces the fluorescence recovery kinetics and the mobile fraction of PHYB-CFP in PBs, indicative of a gel-like state (Fig. 1g). Because even in *gPBC-25*, PHYB-CFP was expressed at a level 7-fold higher than that of endogenous PHYB (Fig. 1c), these results may suggest that changes in PHYB abundance under physiological concentrations may change both PB size and dynamics. Another unexpected result is that increasing PHYB abundance elicited a biphasic PIF5 response. Theoretically, increasing PHYB in a LLPS system should only enhance the amount of PHYB in PBs but not in the nucleoplasm and therefore should generate a linear response. The biphasic response suggests that the cytoplasmic PHYB increased in *gPBC-25* to promote PIF5 degradation, similar to the scenario in the low light condition in *mCherry-PIF5ox/PBC*. These results may suggest that at the physiological PHYB concentration, PBs can form below the critical concentration for PHYB LLPS and therefore require a complex mechanism beyond LLPS.

This study reveals a novel light signaling mechanism in which the condensation of PHYB phase separates two opposing signaling actions: PIF5 stabilization in PBs and PIF5 degradation in the surrounding nucleoplasm. This represents an environmentally sensitive counterbalancing

mechanism that titrates nucleoplasmic PIF5 and its signaling output. This PB-enabled signaling mechanism provides the framework for regulating a plethora of PHYB-interacting signaling molecules in diverse plant environmental responses. We propose that this PB function likely represents a general function of biomolecular condensates to allow distinct variations of a cellular process or signaling pathway to coexist and interact to generate dynamically adjustable integrated outputs within a single subcellular space.

METHODS

Plant materials, growth conditions, and hypocotyl measurements

The *Arabidopsis* Columbia ecotype (Col-0) was used throughout this study. The *phyB-9*[75], *pifq* (Col-0)[76] and *pif5-3* (SALK_087012)[77] mutants, as well as the *PBC* line[32], were previously described. The *gPBC-25*, *gPBC-29*, *mCherry-PIF5/pif5-3* (*#8* and *#9*) and *mCherry-PIF5/PBC* (*#1* and *#9*) transgenic lines were generated in this study. Seeds were surface sterilized with one wash of 70% ethanol followed by a treatment in 32% bleach with 0.03% TritonX-100 for 15 min. The seeds were then washed at least four times with sterile ddH_2O and plated on half-strength Murashige and Skoog media with Gamborg's vitamins (MSP06, Caisson Laboratories, Smithfield, UT), 0.5 mM MES (pH 5.7), and 0.8% (w/v) agar. Seeds were stratified in the dark at 4°C for five days before treatment with specific light conditions and temperatures in an LED chamber (Percival Scientific, Perry, IA). Seedlings grown in the dark were exposed to 10 μmol m^{-2} s^{-1} FR light for 3 h immediately after stratification to induce germination and were then kept in the dark at 21°C for 96 h. Fluence rates of light were measured using an Apogee PS-200 spectroradiometer (Apogee Instruments, Logan, UT) and SpectraWiz® spectroscopy software (StellarNet, Tampa, FL). Images of representative seedlings

were taken using a Leica M165 FC stereo microscope (Leica Microsystems, Deerfield, IL) and processed using Adobe Photoshop CC (Adobe, San Jose, CA). For hypocotyl measurements, seedlings were scanned with an Epson Perfection V700 photo scanner (Epson America, Los Alamitos, CA), and hypocotyl length was measured using NIH ImageJ software.

Plasmid construction and generation of transgenic lines

To generate the *gPBC* lines, genomic *PHYB* DNA with *CFP* inserted in-frame before the stop codon was cloned into *pJHA212G*[78]. The resulting construct was transformed into *phyB-9*. To generate *mCherry-PIF5/pif5-3* lines, a 2.3-kb genomic DNA fragment encompassing the *PIF5* promoter region, 5' UTR, and the first two codons was amplified using PCR and subcloned with 4× *Myc*, *mCherry-2-L* and the *PIF5* coding sequence into *pJHA212G*[78] containing an *rbcS* terminator using Gibson Assembly (New England Biolabs, Ipswich, MA). The resulting construct was transformed into *pif5-3*. To generate *mCherry-PIF5/PBC* lines, a 1.2-kb *UBQ10* promoter was amplified using PCR and subcloned with 3× *HA*, *mCherry-2-L* and the *PIF5* coding sequence into *pJHA212B*[78] containing an *rbcS* terminator using Gibson Assembly. The resulting construct was transformed into *PBC*. The primers used for plasmid construction in this study are listed in Supplementary Table 1.

Protein extraction and immunoblotting

Total protein was extracted from *Arabidopsis* seedlings grown under the indicated conditions. To measure protein degradation kinetics, seedlings were vacuum infiltrated for 15 min with PBS containing 200 μM cycloheximide and then collected at the indicated time points. Plant tissues were ground in liquid nitrogen and resuspended in extraction buffer containing

100 mM Tris-HCl pH 7.5, 100 mM NaCl, 5% SDS, 5 mM EDTA pH 8.0, 20 mM dithiothreitol, 20% glycerol, 142 mM β-mercaptoethanol, 2 mM phenylmethylsulfonyl fluoride, 1× cOmplete™ EDTA-free Protease Inhibitor Cocktail (Sigma-Aldrich, St. Louis, MO), 80 μM MG132, 80 μM MG115, 1% phosphatase inhibitor cocktail 3 (Sigma-Aldrich, St. Louis, MO), 10 mM N-ethylmaleimide (NEM), 2 mM sodium orthovanadate (Na_3OV_4), 25 mM β-glycerophosphate disodium salt hydrate, 10 mM NaF, and 0.01% bromophenol blue. Protein extracts were boiled for 10 min and then centrifuged at 20,000 × *g* for 10 min at room temperature. Protein extracts were separated via 12% SDS-PAGE, transferred to a PVDF membrane, probed with the indicated primary antibodies, and then incubated with HRP-conjugated secondary antibodies. Rabbit anti-PIF5 polyclonal antibody (AS12 2112, Agrisera, Vännäs, Sweden) was used at a 1:1000 dilution. Mouse anti-PHYB monoclonal antibody (a gift from Dr. Akira Nagatani) was used at a 1:2000 dilution. Goat anti-mouse (1706516, Bio-Rad Laboratories, Hercules, CA) and goat anti-rabbit (1706515, Bio-Rad Laboratories, Hercules, CA) secondary antibodies were used at a 1:5000 dilution. Signals were detected via SuperSignal West Dura Extended Duration Chemiluminescent Substrate (Thermo Fisher Scientific, Waltham, MA).

Immunofluorescence staining

Whole-mount immunofluorescence staining was performed as described previously with the following modifications[72,79]. Seedlings were fixed in 4% (v/v) paraformaldehyde (15710, Electron Microscopy Sciences, Hatfield, PA), dehydrated, and mounted on slides[72,79]. All subsequent steps were performed in a 55-μL SecureSeal chamber (621505, Grace Bio-Labs, Bend, OR). Myc-tagged mCherry-PIF5 was detected using a rabbit anti-Myc polyclonal antibody (2272, Cell Signaling Technology, Danvers, MA) as the primary antibody at 1:100 dilution and a

donkey anti-rabbit AlexaFluor 555 antibody (A31572, Thermo Fisher Scientific, Waltham, MA) as the secondary antibody at 1:1000 dilution. PHYB was detected using a mouse monoclonal antibody (a gift from Akira Nagatani, 1:100 dilution) as the primary antibody and a donkey anti-mouse AlexaFluor 488 antibody (A21202, Thermo Fisher Scientific, Waltham, MA, 1:1,000 dilution) as the secondary antibody. Nuclei were counterstained with 3.6 μM 4′,6-diamidino-2-phenylindole (DAPI). Samples were mounted using ProLong Gold Antifade Mountant (Thermo Fisher Scientific, Waltham, MA) and left to cure overnight in the dark before confocal analysis.

Seedling preparation for PB analysis using confocal microscopy

Seedlings were fixed following a previously described protocol with slight modifications[80]. Seedlings were fixed under vacuum with 1% (v/v) paraformaldehyde in PBS for 10 min. After quenching with 50 mM NH_4Cl, the fixed seedlings were permeabilized with 0.2% Triton X-100 in PBS, and nuclei were stained with 3.6 μM DAPI in PBS for 10 min. Seedlings were washed with PBS before being mounted on a slide using Prolong Diamond Antifade Mountant (Thermo Fisher Scientific, Waltham, MA). The slides were left to cure overnight in the dark before being sealed with nail polish and stored at 4°C. For live-cell imaging, seedlings were mounted using PBS. The slides were transported to the microscope in an aluminum foil-wrapped petri dish, and nuclei were imaged within 5 min after mounting.

Fluorescence microscopy and imaging analysis

For immunofluorescence staining experiments (Fig. 2d) and PB quantification and co-localization in mCherry-PIF5/PBC experiments (Figs. 4d,e and 5c-e) , three-dimensional image stacks of individual nuclei of cotyledon pavement epidermal cells were imaged using a Zeiss LSM800 confocal microscope with a ×100/1.4 Plan-Apochromat oil-immersion objective (Carl

Zeiss AG, Jena, Germany). Alexa 488 was monitored using 488 nm excitation and 490-561 nm bandpass detector settings. DAPI was monitored with 353 nm excitation and 410-470 nm bandpass detector settings. Deconvolution (nearest neighbor) was performed and the maximum projection of image stacks (Z-stack interval 0.7 μm) was generated using Zeiss ZEN 2.3 software (Carl Zeiss AG, Jena, Germany). Representative images were exported as TIFF files and processed using Adobe Photoshop CC (Adobe, San Jose, CA). To measure the PB diameter, the boundary of the PB peak was defined as the point where the fluorescence intensity was half of the peak value.

For the *gPBC-25*, *gPBC-29*, and *PBC* PB analysis in Fig.1 e-f, and live-cell imaging (Fig. 4f) three-dimensional image stacks of individual nuclei from cotyledon epidermal or upper hypocotyl epidermal cells were imaged using a Zeiss Axio Observer.Z1 inverted microscope equipped with a Plan-Apochromat 100x/1.4 oil-immersion objective and an Axiocam mono camera (Carl Zeiss, Jena, Germany). Fluorescence was detected using a broad spectrum X-Cite 120LED Boost high-power LED illumination system (Excelitas Technologies, Walham, MA) and the following Zeiss filter sets: DAPI, excitation 365 nm, emission 445/50 nm/nm (Zeiss Filter Set 49); CFP, excitation 436/25 nm/nm, emission 480/40 nm/nm (Filter set 47 HE); mCherry, excitation 550/25 nm/nm, emission 605/70 nm/nm (Zeiss Filter set 43 HE). Image stacks with a Z-step size of 0.24 μm were subjected to iterative classic maximum likelihood estimation deconvolution using Huygens Essential (Scientific Volume Imaging, Hilversum, Netherlands). The Object Analyzer tool was used to threshold the image and to calculate volume of the PBs and was manually adjusted to best match the image.

The partitioning of PHYB-CFP in PBs was measured using the Object Analyzer tool in Huygens Essential (Scientific Volume Imaging, Hilversum, Netherlands). The threshold and

objects were manually adjusted in two channels to best match the image. The program renders a 3D model of all the CFP detected within the nucleus, which is detected by the DAPI channel. One channel was for CFP (PHYB), and the other channel was for DAPI (whole nucleus). The total CFP signal in PBs was calculated from the sum of the intensity values of all voxels in each modeled PB. The total CFP signal within the nucleus (photobody and nucleoplasm) was calculated by the software as the sum of the intensity values of all voxels of the CFP signal within the DAPI channel. Then, the percentage of CFP partitioned to PBs was manually calculated (photobody CFP total / total CFP in the nucleus x 100).

For FRAP experiments, seedlings were mounted in PBS and placed onto a Zeiss LSM800 confocal microscope with a C-Apochromat 63×/1.2 W autocorr M27 objective (Carl Zeiss AG, Jena, Germany). For the *gPBC-25* and *PBC* experiments, PHYB-CFP was monitored using 405 nm excitation and 490-561 nm bandpass detector settings. Images were acquired at 2.7× magnification, the image format was 512 × 512 pixels, and the pinhole was set at 97 μm. One image was taken pre-bleach, followed by 6 iterations of photobleaching at 85% with the 405 nm laser. Images after bleaching were collected using low laser intensities and were taken at 4 s intervals for 18 cycles. For the *mCherry-PIF5/PBC* experiments, PHYB-CFP was monitored using 405 nm excitation and 490-561 nm bandpass detector settings, and mCherry-PIF5 was excited with a 561 nm laser and observed using a 560-630 nm bandpass emission. Images were acquired at 2.7× zoom, the image format was 512 × 512 pixels, and the pinhole was 121 μm. One image was taken pre-bleach, followed by 8 iterations of photobleaching at 50-60% with the 405 nm laser intensity and 85% with the 561 nm laser. Images after bleaching were collected using low laser intensities and were taken at 6 s intervals for 20 cycles. FRAP curve analyses were performed by setting the time of bleach to zero. Normalization was performed by taking the sum

of intensity of the ROI, subtracting the background, and setting the initial pre-bleach intensity to 1. Data were fitted to a one-phase exponential curve, and MF and $t_{1/2}$ were calculated using Prism 10 (GraphPad Software, Boston, MA).

RNA extraction and quantitative real-time PCR

Total RNA from seedlings was isolated using a Quick-RNA MiniPrep kit with on-column DNase I treatment (Zymo Research, Irvine, CA). cDNA was synthesized using Oligo(dT) primers and 1 μg total RNA via a Superscript II First-Strand cDNA Synthesis Kit (Thermo Fisher Scientific, Waltham, MA). qRT-PCR was performed with iQ SYBR Green Supermix (Bio-Rad Laboratories, Hercules, CA) using a LightCycler 96 System (Roche, Basel, Switzerland). The transcript level of each gene was normalized to that of *PP2A*. The statistical analyses were performed using one-way analysis of variance (ANOVA) with post hoc Tukey's HSD using Prism 10 (GraphPad Software, Boston, MA). The primers for qRT-PCR analysis used in this study are listed in Supplementary Table 2.

DATA AVAILABILITY

Arabidopsis mutants and transgenic lines, as well as plasmids generated during the current study, are available from the corresponding author upon reasonable request.

REFERENCES

1. Shaw, P. J. & Brown, J. W. S. Plant nuclear bodies. *Curr. Opin. Plant Biol.* **7**, 614–620 (2004).
2. Mao, Y. S., Zhang, B. & Spector, D. L. Biogenesis and function of nuclear bodies. *Trends*

Genet. **27**, 295–306 (2011).

3. Belmont, A. S. Nuclear compartments: an incomplete primer to nuclear compartments, bodies, and genome organization relative to nuclear architecture. *Cold Spring Harb. Perspect. Biol.* **14**, (2022).
4. Banani, S. F., Lee, H. O., Hyman, A. A. & Rosen, M. K. Biomolecular condensates: organizers of cellular biochemistry. *Nat. Rev. Mol. Cell Biol.* **18**, 285–298 (2017).
5. Emenecker, R. J., Holehouse, A. S. & Strader, L. C. Biological phase separation and biomolecular condensates in plants. *Annu. Rev. Plant Biol.* **72**, 17–46 (2021).
6. Fogal, V. *et al.* Regulation of p53 activity in nuclear bodies by a specific PML isoform. *EMBO J.* **19**, 6185–6195 (2000).
7. Liebl, M. C. & Hofmann, T. G. Regulating the p53 tumor suppressor network at PML biomolecular condensates. *Cancers* **14**, (2022).
8. Van Buskirk, E. K., Decker, P. V. & Chen, M. Photobodies in light signaling. *Plant Physiol.* **158**, 52–60 (2012).
9. Pardi, S. A. & Nusinow, D. A. Out of the dark and into the light: A new view of phytochrome photobodies. *Front. Plant Sci.* **12**, 732947 (2021).
10. Ronald, J. & Davis, S. J. Focusing on the nuclear and subnuclear dynamics of light and circadian signalling. *Plant Cell Environ.* **42**, 2871–2884 (2019).
11. Shi, H. & Zhong, S. Light and temperature perceptions go through a phase separation. *Curr. Opin. Plant Biol.* **74**, 102397 (2023).
12. Rockwell, N. C., Su, Y.-S. & Lagarias, J. C. Phytochrome structure and signaling mechanisms. *Annu. Rev. Plant Biol.* **57**, 837–858 (2006).
13. Burgie, E. S. & Vierstra, R. D. Phytochromes: an atomic perspective on photoactivation and

signaling. *Plant Cell* **26**, 4568–4583 (2014).

14. Chen, M., Chory, J. & Fankhauser, C. Light signal transduction in higher plants. *Annu. Rev. Genet.* **38**, 87–117 (2004).
15. Klose, C., Nagy, F. & Schäfer, E. Thermal reversion of plant phytochromes. *Mol Plant* **13**, (2020).
16. Legris, M. *et al.* Phytochrome B integrates light and temperature signals in Arabidopsis. *Science* **354**, 897–900 (2016).
17. Jung, J.-H. *et al.* Phytochromes function as thermosensors in Arabidopsis. *Science* **354**, 886–889 (2016).
18. Delker, C., Quint, M. & Wigge, P. A. Recent advances in understanding thermomorphogenesis signaling. *Curr. Opin. Plant Biol.* **68**, 102231 (2022).
19. Legris, M., Ince, Y. Ç. & Fankhauser, C. Molecular mechanisms underlying phytochrome-controlled morphogenesis in plants. *Nat Commun* **10**, (2019).
20. Chen, M. & Chory, J. Phytochrome signaling mechanisms and the control of plant development. *Trends Cell Biol.* **21**, 664–671 (2011).
21. Kircher, S. *et al.* Light quality-dependent nuclear import of the plant photoreceptors phytochrome A and B. *Plant Cell* **11**, 1445–1456 (1999).
22. Yamaguchi, R., Nakamura, M., Mochizuki, N., Kay, S. A. & Nagatani, A. Light-dependent translocation of a phytochrome B-GFP fusion protein to the nucleus in transgenic Arabidopsis. *J. Cell Biol.* **145**, 437–445 (1999).
23. Van Buskirk, E. K., Reddy, A. K., Nagatani, A. & Chen, M. Photobody localization of phytochrome B is tightly correlated with prolonged and light-dependent inhibition of hypocotyl elongation in the dark. *Plant Physiol.* **165**, 595–607 (2014).

24. Murcia, G., Enderle, B., Hiltbrunner, A. & Casal, J. J. Phytochrome B and PCH1 protein dynamics store night temperature information. *Plant J.* **105**, 22–33 (2021).

25. Huang, H. *et al.* PCH1 integrates circadian and light-signaling pathways to control photoperiod-responsive growth in Arabidopsis. *Elife* **5**, e13292 (2016).

26. Trupkin, S. A., Legris, M., Buchovsky, A. S., Tolava Rivero, M. B. & Casal, J. J. Phytochrome B nuclear bodies respond to the low red to far-red ratio and to the reduced irradiance of canopy shade in Arabidopsis. *Plant Physiol.* **165**, 1698–1708 (2014).

27. Chen, M., Schwab, R. & Chory, J. Characterization of the requirements for localization of phytochrome B to nuclear bodies. *Proc. Natl. Acad. Sci. U. S. A.* **100**, 14493–14498 (2003).

28. Chen, M. *et al.* Arabidopsis HEMERA/pTAC12 initiates photomorphogenesis by phytochromes. *Cell* **141**, 1230–1240 (2010).

29. Hahm, J., Kim, K., Qiu, Y. & Chen, M. Increasing ambient temperature progressively disassembles Arabidopsis phytochrome B from individual photobodies with distinct thermostabilities. *Nat. Commun.* **11**, 1660 (2020).

30. Su, Y.-S. & Lagarias, J. C. Light-independent phytochrome signaling mediated by dominant GAF domain tyrosine mutants of Arabidopsis phytochromes in transgenic plants. *Plant Cell* **19**, 2124–2139 (2007).

31. Viczián, A. *et al.* Differential phosphorylation of the N-terminal extension regulates phytochrome B signaling. *New Phytol.* **225**, 1635–1650 (2020).

32. Chen, M., Tao, Y., Lim, J., Shaw, A. & Chory, J. Regulation of phytochrome B nuclear localization through light-dependent unmasking of nuclear-localization signals. *Curr. Biol.* **15**, 637–642 (2005).

33. Zhang, J., Stankey, R. J. & Vierstra, R. D. Structure-guided engineering of plant

phytochrome B with altered photochemistry and light signaling. *Plant Physiol.* **161**, 1445–1457 (2013).

34. Matsushita, T., Mochizuki, N. & Nagatani, A. Dimers of the N-terminal domain of phytochrome B are functional in the nucleus. *Nature* **424**, 571–574 (2003).
35. Klose, C. *et al.* Systematic analysis of how phytochrome B dimerization determines its specificity. *Nat Plants* **1**, 15090 (2015).
36. Qiu, Y. *et al.* Mechanism of early light signaling by the carboxy-terminal output module of Arabidopsis phytochrome B. *Nat. Commun.* **8**, 1905 (2017).
37. Chen, D. *et al.* Integration of light and temperature sensing by liquid-liquid phase separation of phytochrome B. *Mol. Cell* **82**, 3015–3029.e6 (2022).
38. Fonin, A. V. *et al.* Photo-dependent membrane-less organelles formed from plant phyB and PIF6 proteins in mammalian cells. *Int. J. Biol. Macromol.* **176**, 325–331 (2021).
39. Beyer, H. M. *et al.* Red light-regulated reversible nuclear localization of proteins in mammalian cells and zebrafish. *ACS Synth. Biol.* **4**, 951–958 (2015).
40. Cheng, M.-C., Kathare, P. K., Paik, I. & Huq, E. Phytochrome Signaling Networks. *Annu. Rev. Plant Biol.* **72**, 217–244 (2021).
41. Lee, N. & Choi, G. Phytochrome-interacting factor from Arabidopsis to liverwort. *Curr. Opin. Plant Biol.* **35**, 54–60 (2017).
42. Al-Sady, B., Ni, W., Kircher, S., Schäfer, E. & Quail, P. H. Photoactivated phytochrome induces rapid PIF3 phosphorylation prior to proteasome-mediated degradation. *Mol. Cell* **23**, 439–446 (2006).
43. Shen, Y., Khanna, R., Carle, C. M. & Quail, P. H. Phytochrome induces rapid PIF5 phosphorylation and degradation in response to red-light activation. *Plant Physiol.* **145**,

1043–1051 (2007).

44. Lorrain, S., Allen, T., Duek, P. D., Whitelam, G. C. & Fankhauser, C. Phytochrome-mediated inhibition of shade avoidance involves degradation of growth-promoting bHLH transcription factors. *Plant J.* **53**, 312–323 (2008).
45. Shen, H., Moon, J. & Huq, E. PIF1 is regulated by light-mediated degradation through the ubiquitin-26S proteasome pathway to optimize photomorphogenesis of seedlings in Arabidopsis. *Plant J.* **44**, 1023–1035 (2005).
46. Ni, W. *et al.* PPKs mediate direct signal transfer from phytochrome photoreceptors to transcription factor PIF3. *Nat. Commun.* **8**, 15236 (2017).
47. Ni, W. *et al.* A mutually assured destruction mechanism attenuates light signaling in Arabidopsis. *Science* **344**, 1160–1164 (2014).
48. Dong, J. *et al.* Light-dependent degradation of PIF3 by SCFEBF1/2 promotes a photomorphogenic response in Arabidopsis. *Curr. Biol.* **27**, 2420–2430.e6 (2017).
49. Sheerin, D. J. *et al.* Light-activated phytochrome A and B interact with members of the SPA family to promote photomorphogenesis in Arabidopsis by reorganizing the COP1/SPA complex. *Plant Cell* **27**, 189–201 (2015).
50. Lu, X.-D. *et al.* Red-light-dependent interaction of phyB with SPA1 promotes COP1-SPA1 dissociation and photomorphogenic development in Arabidopsis. *Mol. Plant* **8**, 467–478 (2015).
51. Saijo, Y. *et al.* The COP1-SPA1 interaction defines a critical step in phytochrome A-mediated regulation of HY5 activity. *Genes Dev.* **17**, 2642–2647 (2003).
52. Podolec, R. & Ulm, R. Photoreceptor-mediated regulation of the COP1/SPA E3 ubiquitin ligase. *Curr. Opin. Plant Biol.* **45**, 18–25 (2018).

53. Chen, M. *et al.* Arabidopsis HEMERA/pTAC12 initiates photomorphogenesis by phytochromes. *Cell* **141**, 1230–1240 (2010).

54. Qiu, Y., Li, M., Kim, R. J.-A., Moore, C. M. & Chen, M. Daytime temperature is sensed by phytochrome B in Arabidopsis through a transcriptional activator HEMERA. *Nat. Commun.* **10**, 140 (2019).

55. Pham, V. N., Kathare, P. K. & Huq, E. Dynamic regulation of PIF5 by COP1-SPA complex to optimize photomorphogenesis in Arabidopsis. *Plant J.* **96**, 260–273 (2018).

56. Qiu, Y. *et al.* RCB initiates Arabidopsis thermomorphogenesis by stabilizing the thermoregulator PIF4 in the daytime. *Nat. Commun.* **12**, 2042 (2021).

57. Kim, C. *et al.* Phytochrome B photobodies are comprised of phytochrome B and its primary and secondary interacting proteins. *Nat. Commun.* **14**, 1708 (2023).

58. Huang, H. *et al.* Identification of evening complex associated proteins in Arabidopsis by affinity purification and mass spectrometry. *Mol. Cell. Proteomics* **15**, 201–217 (2016).

59. Kaiserli, E. *et al.* Integration of light and photoperiodic signaling in transcriptional nuclear foci. *Dev. Cell* **35**, 311–321 (2015).

60. Bauer, D. *et al.* Constitutive photomorphogenesis 1 and multiple photoreceptors control degradation of phytochrome interacting factor 3, a transcription factor required for light signaling in Arabidopsis. *Plant Cell* **16**, 1433–1445 (2004).

61. Galvão, R. M. *et al.* Photoactivated phytochromes interact with HEMERA and promote its accumulation to establish photomorphogenesis in Arabidopsis. *Genes Dev.* **26**, 1851–1863 (2012).

62. Qiu, Y. *et al.* HEMERA couples the proteolysis and transcriptional activity of PHYTOCHROME INTERACTING FACTORs in Arabidopsis photomorphogenesis. *Plant*

Cell **27**, 1409–1427 (2015).

63. Yoo, C. Y. *et al.* Phytochrome activates the plastid-encoded RNA polymerase for chloroplast biogenesis via nucleus-to-plastid signaling. *Nat. Commun.* **10**, 2629 (2019).
64. Yang, E. J. *et al.* NCP activates chloroplast transcription by controlling phytochrome-dependent dual nuclear and plastidial switches. *Nat. Commun.* **10**, 2630 (2019).
65. Klosin, A. *et al.* Phase separation provides a mechanism to reduce noise in cells. *Science* **367**, 464–468 (2020).
66. Balleza, E., Kim, J. M. & Cluzel, P. Systematic characterization of maturation time of fluorescent proteins in living cells. *Nat. Methods* **15**, 47–51 (2018).
67. Banani, S. F. *et al.* Compositional control of phase-separated cellular bodies. *Cell* **166**, 651–663 (2016).
68. Jang, I.-C., Henriques, R., Seo, H. S., Nagatani, A. & Chua, N.-H. Arabidopsis PHYTOCHROME INTERACTING FACTOR proteins promote phytochrome B polyubiquitination by COP1 E3 ligase in the nucleus. *Plant Cell* **22**, 2370–2383 (2010).
69. Zhu, L. *et al.* CUL4 forms an E3 ligase with COP1 and SPA to promote light-induced degradation of PIF1. *Nat. Commun.* **6**, 7245 (2015).
70. Paik, I. *et al.* A phyB-PIF1-SPA1 kinase regulatory complex promotes photomorphogenesis in Arabidopsis. *Nat. Commun.* **10**, 4216 (2019).
71. Chen, H. *et al.* Arabidopsis CULLIN4 forms an E3 ubiquitin ligase with RBX1 and the CDD complex in mediating light control of development. *Plant Cell* **18**, 1991–2004 (2006).
72. Willige, B. C. *et al.* PHYTOCHROME INTERACTING FACTORs trigger environmentally responsive chromatin dynamics in plants. *Nat Genet* **53**, 955–961 (2021).
73. Majee, M. *et al.* KELCH F-BOX protein positively influences Arabidopsis seed

germination by targeting PHYTOCHROME-INTERACTING FACTOR1. *Proc. Natl. Acad. Sci. U. S. A.* **115**, E4120–E4129 (2018).

74. Zhang, B. *et al.* BLADE-ON-PETIOLE proteins act in an E3 ubiquitin ligase complex to regulate PHYTOCHROME INTERACTING FACTOR 4 abundance. *Elife* **6**, (2017).
75. Reed, J. W., Nagpal, P., Poole, D. S., Furuya, M. & Chory, J. Mutations in the gene for the red/far-red light receptor phytochrome B alter cell elongation and physiological responses throughout Arabidopsis development. *Plant Cell* **5**, 147–157 (1993).
76. Leivar, P. *et al.* Multiple phytochrome-interacting bHLH transcription factors repress premature seedling photomorphogenesis in darkness. *Curr. Biol.* **18**, 1815–1823 (2008).
77. Khanna, R. *et al.* The basic helix-loop-helix transcription factor PIF5 acts on ethylene biosynthesis and phytochrome signaling by distinct mechanisms. *Plant Cell* **19**, 3915–3929 (2007).
78. Yoo, S. Y. *et al.* The 35S promoter used in a selectable marker gene of a plant transformation vector affects the expression of the transgene. *Planta* **221**, 523–530 (2005).
79. Feng, C.-M., Qiu, Y., Van Buskirk, E. K., Yang, E. J. & Chen, M. Light-regulated gene repositioning in Arabidopsis. *Nat. Commun.* **5**, 3027 (2014).
80. Yoo, C. Y., Williams, D. & Chen, M. Quantitative Analysis of Photobodies. *Methods Mol. Biol.* **2026**, 135–141 (2019).

ACKNOWLEDGEMENTS

We thank Akira Nagatani (Kyoto University) for providing anti-PHYB antibodies. We thank Elise Pasoreck for valuable suggestions and comments on the manuscript. We are grateful to Xuemei Chen for her support of D.F. in a collaborative project on thermomorphogenesis. This

work was supported by National Institute of General Medical Sciences grant R01GM087388 to M.C.

AUTHOR CONTRIBUTIONS

R.J.K., D.F., J.H., K.K., J.D. and M.C. conceived of the original research plan; M.C. supervised the experiments; R.J.K., D.F., J.H., K.K., J.D. and M.C. performed the experiments; R.J.K., D.F., J.H., K.K., J.D. and M.C. analyzed the data; R.J.K., D.F., J.H., and M.C. wrote the article with contributions from all authors.

COMPETING INTERESTS

The authors declare no competing interests.

FIGURE LEGENDS

Fig. 1. Increasing PHYB abundance alters PB size and dynamics. a Images of 4-d-old *phyB-9,* Col-0, *gPBC-25, gPBC-29* and *PBC* seedlings grown under 10 μmol m^{-2} s^{-1} R light at 21°C. **b** Hypocotyl length measurements of the seedlings shown in **a**. Error bars represent the s.d. (n > 50 seedlings); the centers of the error bars indicate the mean. Different letters denote statistically significant differences in hypocotyl length (ANOVA, Tukey's HSD, $p \leq 0.05$). **c** Immunoblots showing the PHYB levels in the seedlings described in **a**. Actin was used as a loading control. The relative endogenous PHYB and PHYB-CFP levels normalized to the corresponding levels of actin are shown. The immunoblot experiments were independently repeated three times with similar results. **d** Confocal images showing representative PHYB-CFP PB patterns in cotyledon pavement epidermal cells from 4-d-old *gPBC-25, gPBC-29* and *PBC* seedlings grown under 10

μmol m^{-2} s^{-1} R light at 21ºC. Scale bars are equal to 2 μm. **e** Quantification of the PB volume in cotyledon epidermal cells from *gPBC-25, gPBC-29* and *PBC* as shown in **d**. Different letters denote statistically significant differences in volume (ANOVA, Tukey's HSD, $p \leq 0.05$). **f** Quantification of the percentage of PHYB partitioned to PBs based on the total PHYB signal within the nuclei of *gPBC-25*, *gPBC-29* and *PBC* as shown in **d**. Box and whisker plots showing the percent of PHYB partitioned to PBs per nucleus. Different letters denote statistically significant differences in percentage (ANOVA, Tukey's HSD, $p \leq 0.05$). For **e** and **f**, the numbers indicate the mean values. In the box and whisker plots, the boxes represent the 25th to 75th percentiles, and the bars are equal to the mean. **g** Results of FRAP experiments showing normalized fluorescence recovery plotted over time for PHYB-CFP in PBs of pavement cell nuclei from 4-d-old *gPBC-25* (black) and *PBC* (magenta) seedlings grown under 50 μmol m^{-2} s^{-1} R light. Values represent the mean, and error bars represent the s.e. of the mean of three biological replicates. The solid lines represent an exponential fit of the data. MF: mobile fraction; $t_{1/2}$ represents the half-time of fluorescence recovery.

Fig. 2. mCherry-PIF5 is a short-lived protein localized in PBs. a Images of 4-d-old seedlings of Col-0, *pif5-3* and two *mCherry-PIF5/pif5-3* (*#8* and *#9*) lines grown under 50 μmol m^{-2} s^{-1} R light at 16ºC or 27ºC. **b** Hypocotyl length measurements of the seedlings described in **a**. The open and gray bars represent hypocotyl length measurements at 16ºC and 27ºC, respectively. The percent increase in hypocotyl length (mean ± s.d., n = 90) is shown. The black numbers above the Col-0 data represent the increase in hypocotyl length (mean ± s.d., n = 3 biological replicates) at 27ºC compared to 16ºC. The pink bars show the relative response, which is defined as the hypocotyl response to 27ºC of a mutant or transgenic line relative to that of Col-0 (set at

100%). Error bars for the hypocotyl measurements represent the s.d. (n = 90 seedlings); error bars for the relative responses represent the s.d. of three biological replicates. The centers of the error bars indicate the mean values. Pink numbers show the mean ± s.d. of the relative responses, and different lowercase and uppercase letters denote statistically significant differences in the relative responses and hypocotyl lengths at 27ºC, respectively (ANOVA, Tukey's HSD, $p < 0.05$, n = 3 biological replicates). **c** Immunoblots showing the steady-state levels of PIF5 or mCherry-PIF5 in 4-d-old Col-0, *pif5-3*, and the *mCherry-PIF5* lines (*#8*, *#9*) grown under 50 μmol m^{-2} s^{-1} R light at 16ºC or 27ºC. PIF5 and mCherry-PIF5 were detected using anti-PIF5 antibodies. Actin was used as a loading control. The relative levels of PIF5 or mCherry-PIF5 normalized to actin are shown. The asterisk indicates a nonspecific band. **d** Confocal images showing the colocalization of *mCherry-PIF5* and PHYB in PBs in cotyledon pavement epidermal nuclei from 4-d-old *mCherry-PIF5* line *#8* seedlings grown under 50 μmol m^{-2} s^{-1} R light at 16ºC or 27ºC. PHYB (green) and Myc-tagged *mCherry-PIF5* (red) were labeled via immunofluorescence staining using anti-PHYB and anti-Myc antibodies, respectively. Nuclei were stained with DAPI (blue). Scale bars are equal to 2 μm. **e** Quantification of the colocalization of mCherry-PIF5 foci with PHYB-CFP PBs in the experiments described in **d**. Error bars represent the s.e. of at least three biological replicates.

Fig. 3. Increased PHYB abundance induces a biphasic PIF5 response. a Immunoblots showing PHYB and PIF5 levels in 4-d-old *phyB-9,* Col-0, *gPBC-25, gPBC-29* and *PBC* seedlings grown under 10 μmol m^{-2} s^{-1} R light at 21ºC. 4-d-old dark-grown Col-0 and R-light-grown *pifq* were used as positive and negative controls for PIF5, respectively. Actin was used as a loading control. The asterisk indicates a nonspecific band. The relative PHYB and PIF5 levels,

normalized to the corresponding actin levels, are shown below each lane. The immunoblot experiments were independently repeated three times with similar results. **b** Quantification of the PHYB and PIF5 levels shown in **a**. Error bars represent the s.d. of three independent replicates. The centers of the error bars indicate the mean values. Different lowercase and uppercase letters denote statistically significant differences in the abundance of PHYB and PIF5, respectively (ANOVA, Tukey's HSD, $p < 0.05$, n = 3 biological replicates). **c** qRT-PCR analysis of the transcript levels of *PHYB* and *PIF5* in seedlings shown in **a**. Different lowercase and uppercase letters denote statistically significant differences in *PHYB* and *PIF5* transcripts, respectively (ANOVA, Tukey's HSD, $p < 0.05$, n = 3 biological replicates). **d** Immunoblots showing the degradation kinetics of PIF5 in Col-0, *gPBC-25,* and *PBC*. 4-d-old Col-0, *gPBC-25* and *PBC* seedlings were incubated with cycloheximide and collected at the indicated time points. Total proteins were extracted and subjected to immunoblotting analysis using anti-PIF5 antibodies. Actin was used as a loading control. The asterisk indicates a nonspecific band. The relative PIF5 levels normalized to the corresponding levels of actin are shown. **e** Quantification of the relative PIF5 protein levels shown in **d**. Error bars represent the s.d. of three independent replicates.

Fig. 4. PHYB recruits and stabilizes PIF5 in PBs. a Images of 4-d-old *PBC* and *mCherry-PIF5/PBC* (*#1* and *#9*) seedlings grown under 10 μmol m^{-2} s^{-1} R light at either 16°C or 27°C. **b** Hypocotyl length measurements of the seedings described in **a**. Error bars represent the s.d., and the center represents the mean (n ≥ 32 seedlings). Samples labeled with different letters exhibited statistically significant differences in hypocotyl length (ANOVA, Tukey's HSD, $p \leq 0.05$). **c** Immunoblots showing the steady-state levels of PIF5 or mCherry-PIF5 in 4-d-old *pif5-3*, Col-0, *PBC*, and *mCherry-PIF5* (*#1*, *#9*) seedlings grown under 10 μmol m^{-2} s^{-1} R light at either 16°C or 27°C. PIF5 and mCherry-PIF5 were detected using anti-PIF5 antibodies. Actin was used as a

loading control. The asterisk indicates a nonspecific band. The relative levels of PIF5 and mCherry-PIF5, normalized to the corresponding levels of actin, are shown below each lane. **d** Confocal images showing the colocalization of *mCherry-PIF5* with PHYB-CFP in PBs in cotyledon pavement cells from 4-d-old *mCherry-PIF5/PBC #9* seedlings grown under 10 μmol m^{-2} s^{-1} R light at either 16°C or 27°C. Scale bars are equal to 2 μm. **e** Quantification of the colocalization of mCherry-PIF5 foci with PHYB-CFP PBs in the experiments described in **d**. Error bars represent the s.e. (n = 9 biological replicates for the 16°C samples, n = 7 biological replicates for the 27°C samples), and the center represents the mean. **f** Fluorescence microscope images showing the localization of PHYB-CFP and mCherry-PIF5 in hypocotyl epidermal cells from 4-d-old dark-grown *mCherry-PIF5/PBC #9* seedings. The DIC image shows the nucleus. Scale bars are equal to 5 μm. **g** Immunoblots showing the degradation kinetics of Myc-tagged mCherry-PIF5 in *mCherry-PIF5/pif5-3* and HA-tagged mCherry-PIF5 in *mCherry-PIF5/PBC*. 4-d-old seedlings of *mCherry-PIF5/pif5-3 #8* and *mCherry-PIF5/PBC #9* were incubated with cycloheximide and collected at the indicated time points. Total proteins were extracted and subjected to immunoblotting analysis using anti-PIF5 antibodies. Actin was used as a loading control. The asterisk indicates a nonspecific band. The relative mCherry-PIF5 levels normalized to the corresponding levels of actin are shown. **h** Quantification of the relative mCherry-PIF5 levels shown in **g**. Error bars represent the s.d. of three independent replicates.

Fig. 5. Reducing PB size accelerates PIF5 degradation. a Images of 4-d-old Col-0, *PBC* and *mCherry-PIF5/PBC #9* seedlings grown under either 10 μmol m^{-2} s^{-1} or 0.5 μmol m^{-2} s^{-1} R light. **b** Hypocotyl length measurement of the seedlings described in **a**. Error bars represent the s.d., and the center represents the mean (n = 90 seedlings). Samples labeled with different letters

exhibited statistically significant differences in hypocotyl length (Student's t-test, $p \leq 0.05$). **c** Confocal images showing the PB patterns in cotyledon pavement epidermal cells from the *mCherry-PIF5/PBC* seedlings described in **a**. Scale bars are equal to 2 μm. **d** Quantification of the sizes of the PBs described in **c**. Error bars represent the s.d., and the center represents the mean (n = 53 PBs for the 10 μmol m^{-2} s^{-1} samples, n = 72 for the 0.5 μmol m^{-2} s^{-1} samples). Different letters denote statistically significant differences in PB size (Student's t-test, $p \leq 0.05$). **e** Quantification of the percentage PHYB-CFP PBs with detectable mCherry-PIF5 fluorescence in *mCherry-PIF5/PBC* seedlings grown under 0.5 μmol m^{-2} s^{-1} R light. The error bar represents the s.d., and the center represents the mean (n = 30). **f** Immunoblots of PHYB-CFP, endogenous PIF5 and mCherry-PIF5 in 4-d-old *PBC* and *mCherry-PIF5/PBC #9* seedlings grown under either 10 μmol m^{-2} s^{-1} or 0.5 μmol m^{-2} s^{-1} R light. Actin was used as a control. The relative levels of PHYB-CFP, endogenous PIF5 and mCherry-PIF5, normalized to the corresponding actin levels, are shown under each lane. The asterisk indicates a nonspecific band. **g** Immunoblots showing the degradation kinetics of mCherry-PIF5 in 4-d-old *mCherry-PIF5/PBC #9* seedlings grown under either 10 μmol m^{-2} s^{-1} or 0.5 μmol m^{-2} s^{-1} R light. Seedlings were incubated with cycloheximide and collected at the indicated time points. Total proteins were extracted and subjected to immunoblotting analysis using anti-PIF5 antibodies. Actin was used as a loading control. The relative mCherry-PIF5 levels normalized to the corresponding levels of actin are shown. **h** Results of FRAP experiments showing normalized fluorescence recovery plotted over time for PHYB-CFP in the *mCherry-PIF5/PBC #9* seedlings described in **a**. **i** Results of FRAP experiments showing normalized fluorescence recovery plotted over time for mCherry-PIF5 in the *mCherry-PIF5/PBC #9* seedlings described in **a**. For **h** and **i**, values represent the mean, and error bars represent the s.e. of at least three biological replicates. Solid

lines represent the exponential fit of the data. MF: mobile fraction; $t_{1/2}$ represents the half-time of fluorescence recovery.

Fig. 6. A PB-enabled counterbalancing model for titrating nucleoplasmic PIF5. The condensation of PHYB creates a PIF5-stabilizing environment in PBs to counteract PIF5 degradation in the surrounding nucleoplasm. In the nucleoplasm, PHYB promotes PIF5 degradation by triggering its phosphorylation and ubiquitylation by the $CRL4^{COP1/SPA}$ E3 ubiquitin ligase[43,44,55]. In contrast, PBs stabilize PIF5 because only COP1 and SPAs, but not the CRL4 core, are localized to PBs[25,59,71], and the high concentration of PHYB in PBs disrupts the COP1-SPA complex via distinct interactions of COP1 with PHYB's N-terminal photosensory module and SPAs with PHYB's C-terminal output module[49–51,68,70]. PHYB serves as a scaffold component providing binding sites to recruit PIF5 as a client via direct interaction. Changes in light and temperature directly control the amount of active PHYB and thus the size of PBs to regulate the PB-to-nucleoplasmic partitioning of PIF5 and other PB constituents, thereby enabling an environmentally sensitive counterbalancing system to titrate nucleoplasmic PIF5 and its transcriptional output.

SUPPLEMENTARY INFORMATION

Supplementary Table 1. List of primers used for plasmid construction.

Supplementary Table 2. List of primers used for qRT-PCR experiments.

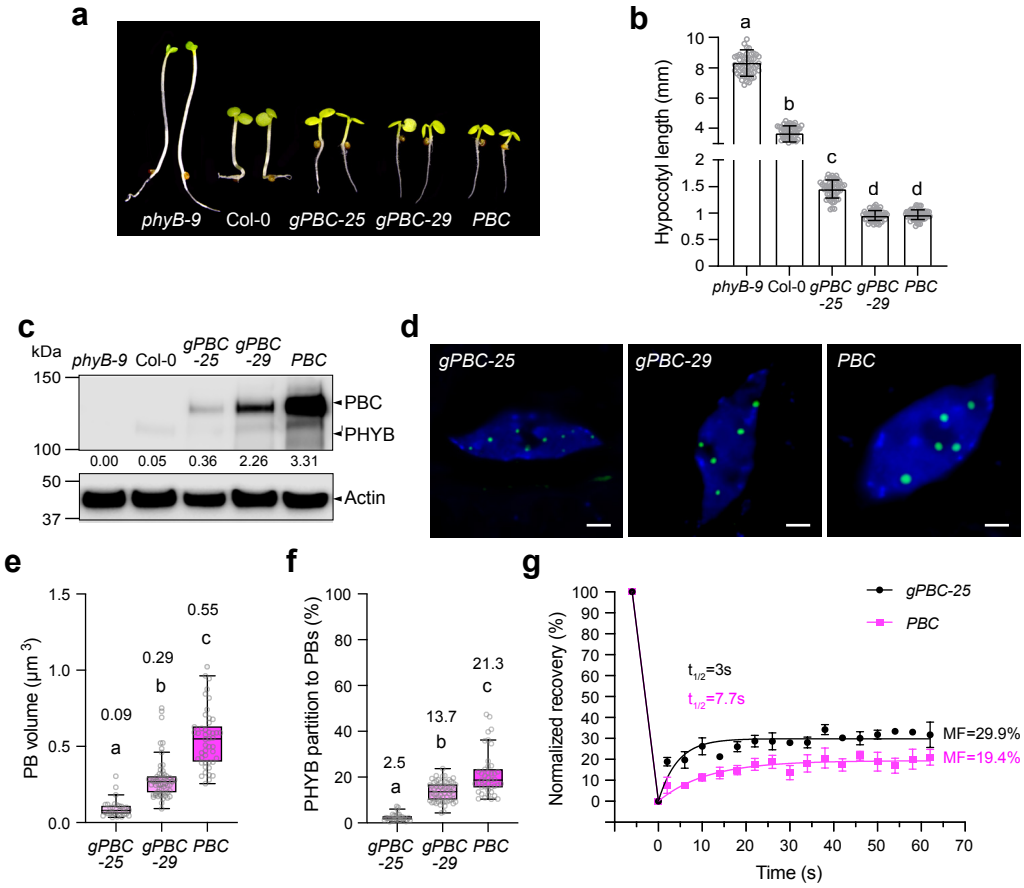

Fig. 1. Increasing PHYB abundance alters PB size and dynamics. a Images of 4-d-old *phyB-9*, Col-0, *gPBC-25*, *gPBC-29* and *PBC* seedlings grown under 10 μmol m^{-2} s^{-1} R light at 21°C. **b** Hypocotyl length measurements of the seedlings shown in **a**. Error bars represent the s.d. (n > 50 seedlings), the centers of the error bars indicate the mean. Different letters denote statistically significant differences in hypocotyl length (ANOVA, Tukey's HSD, $p \leq 0.05$). **c** Immunoblots showing the PHYB levels in the seedlings described in **a**. Actin was used as a loading control. The relative endogenous PHYB and PHYB-CFP levels normalized to the corresponding levels of actin are shown. The immunoblot experiments were independently repeated three times with similar results. **d** Confocal images showing representative PHYB-CFP PB patterns in cotyledon pavement epidermal cells from 4-d-old *gPBC-25*, *gPBC-29* and *PBC* seedlings grown under 10 μmol m^{-2} s^{-1} R light at 21°C. Scale bars are equal to 2 μm. **e** Quantification of the PB volume in cotyledon epidermal cells from *gPBC-25*, *gPBC-29* and *PBC* as shown in **d**. Different letters denote statistically significant differences in volume (ANOVA, Tukey's HSD, $p \leq 0.05$). **f** Quantification of percentage of PHYB partitioned to PBs based on the total PHYB signal within the nuclei of *gPBC-25*, *gPBC-29* and *PBC* as shown in **d**. Box and whisker plots showing the percent of PHYB partitioned to PBs per nucleus. Different letters denote statistically significant differences in percentage (ANOVA, Tukey's HSD, $p \leq 0.05$). For **e** and **f**, the numbers indicate the mean values. In the box and whisker plots, the boxes represent the 25th to 75th percentiles, and the bars are equal to the mean. **g** Results of FRAP experiments showing normalized fluorescence recovery plotted over time for PHYB-CFP in PBs of pavement cell nuclei from 4-d-old *gPBC-25* (black) and *PBC* (magenta) seedlings grown under 50 μmol m^{-2} s^{-1} R light. Values represent the mean, and error bars represent the s.e of the mean of three biological replicates. The solid lines represent an exponential fit of the data. MF: mobile fraction; $t_{1/2}$ represents the half-time of fluorescence recovery.

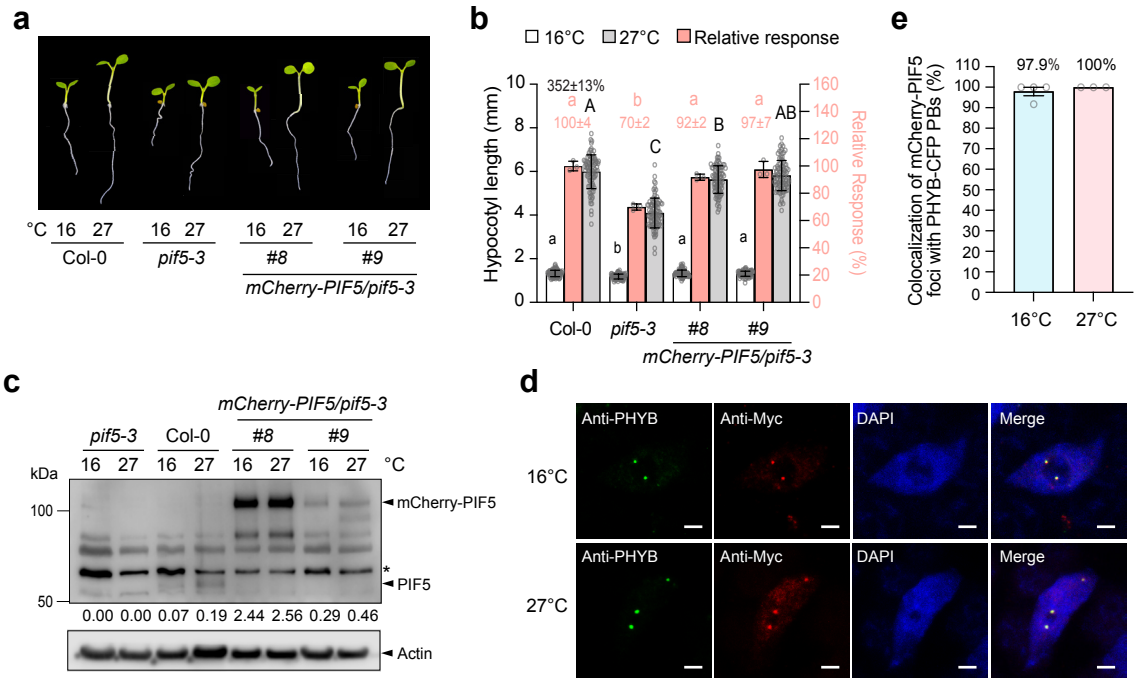

Fig. 2. mCherry-PIF5 is a short-lived protein localized in PBs. a Images of 4-d-old seedlings of Col-0, *pif5-3* and two *mCherry-PIF5/pif5-3* (*#8* and *#9*) lines grown under 50 μmol m^{-2} s^{-1} R light at 16°C or 27°C. **b** Hypocotyl length measurements of the seedlings described in **a**. The open and gray bars represent hypocotyl length measurements at 16°C and 27°C, respectively. The percent increase in hypocotyl length (mean ± s.d., n = 90) is shown. The black numbers above the Col-0 data represent the increase in hypocotyl length (mean ± s.d., n = 3 biological replicates) at 27°C compared to 16°C. The pink bars show the relative response, which is defined as the relative hypocotyl response to 27°C of a mutant or transgenic line compared with that of Col-0 (set at 100%). Error bars for the hypocotyl measurements represent the s.d. (n = 90 seedlings); error bars for the relative responses represent the s.d. of three biological replicates. The centers of the error bars indicate the mean values. Pink numbers show the mean ± s.d. of the relative responses, and different lowercase and uppercase letters denote statistically significant differences in the relative responses and hypocotyl lengths at 27°C, respectively (ANOVA, Tukey's HSD, $p < 0.05$, n = 3 biological replicates). **c** Immunoblots showing the steady-state levels of PIF5 or mCherry-PIF5 in 4-d-old Col-0, *pif5-3*, and the *mCherry-PIF5* lines (*#8*, *#9*) grown under 50 μmol m^{-2} s^{-1} R light at 16°C or 27°C. PIF5 and mCherry-PIF5 were detected using anti-PIF5 antibodies. Actin was used as a loading control. The relative levels of PIF5 or mCherry-PIF5 normalized to actin are shown. The asterisk indicates a non-specific band. **d** Confocal images showing the colocalization of mCherry-PIF5 and PHYB in PBs in cotyledon pavement epidermal nuclei from 4-d-old mCherry-PIF5 line *#8* seedlings grown under 50 μmol m^{-2} s^{-1} R light at 16°C or 27°C. PHYB (green) and Myc-tagged mCherry-PIF5 (red) were labeled via immunofluoresence staining using anti-PHYB and anti-Myc antibodies, respectively. Nuclei were stained with DAPI (blue). Scale bars are equal to 2 μm. **e** Quantification of the colocalization of mCherry-PIF5 foci with PHYB-CFP PBs in the experiments described in **d**. Error bars represent the s.e. of at least three biological replicates.

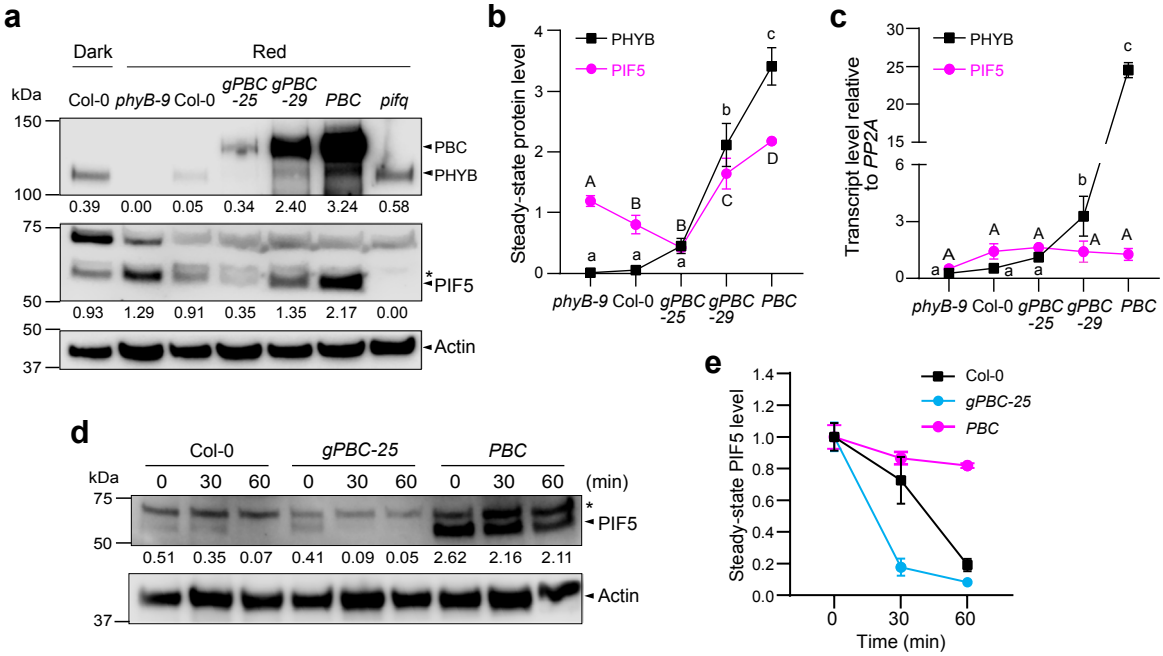

Fig. 3. Increased PHYB abundance induces a biphasic PIF5 response. a Immunoblots showing PHYB and PIF5 levels in 4-d-old *phyB-9*, Col-0, *gPBC-25*, *gPBC-29* and *PBC* seedlings grown under 10 μmol m^{-2} s^{-1} R light at 21°C. 4-d-old dark-grown Col-0 and R-light-grown *pifq* were used as positive and negative controls for PIF5, respectively. Actin was used as a loading control. The asterisk indicates a nonspecific band. The relative PHYB and PIF5 levels, normalized to the corresponding actin levels, are shown below each lane. The immunoblot experiments were independently repeated three times with similar results. **b** Quantification of the PHYB and PIF5 levels shown in **a**. Error bars represent the s.d. of three independent replicates. The centers of the error bars indicate the mean values. Different lowercase and uppercase letters denote statistically significant differences in the abundance of PHYB and PIF5, respectively (ANOVA, Tukey's HSD, $p < 0.05$, n = 3 biological replicates). **c** qRT-PCR analysis of the transcript levels of PHYB and PIF5 in seedlings shown in **a**. Different lowercase and uppercase letters denote statistically significant differences in PHYB and PIF5 transcripts, respectively (ANOVA, Tukey's HSD, $p < 0.05$, n = 3 biological replicates). **d** Immunoblots showing the degradation kinetics of PIF5 in Col-0, *gPBC-25* and *PBC*. 4-d-old Col-0, *gPBC-25* and *PBC* seedlings were incubated with cycloheximide and collected at the indicated time points. Total proteins were extracted at the indicated times and subjected to immunoblotting analysis using anti-PIF5 antibodies. Actin was used as a loading control. The asterisk indicates a nonspecific band. The relative PIF5 levels normalized to the corresponding levels of actin are shown. **e** Quantification of the PIF5 levels shown in **d**. Error bars represent the s.d. of three independent replicates.

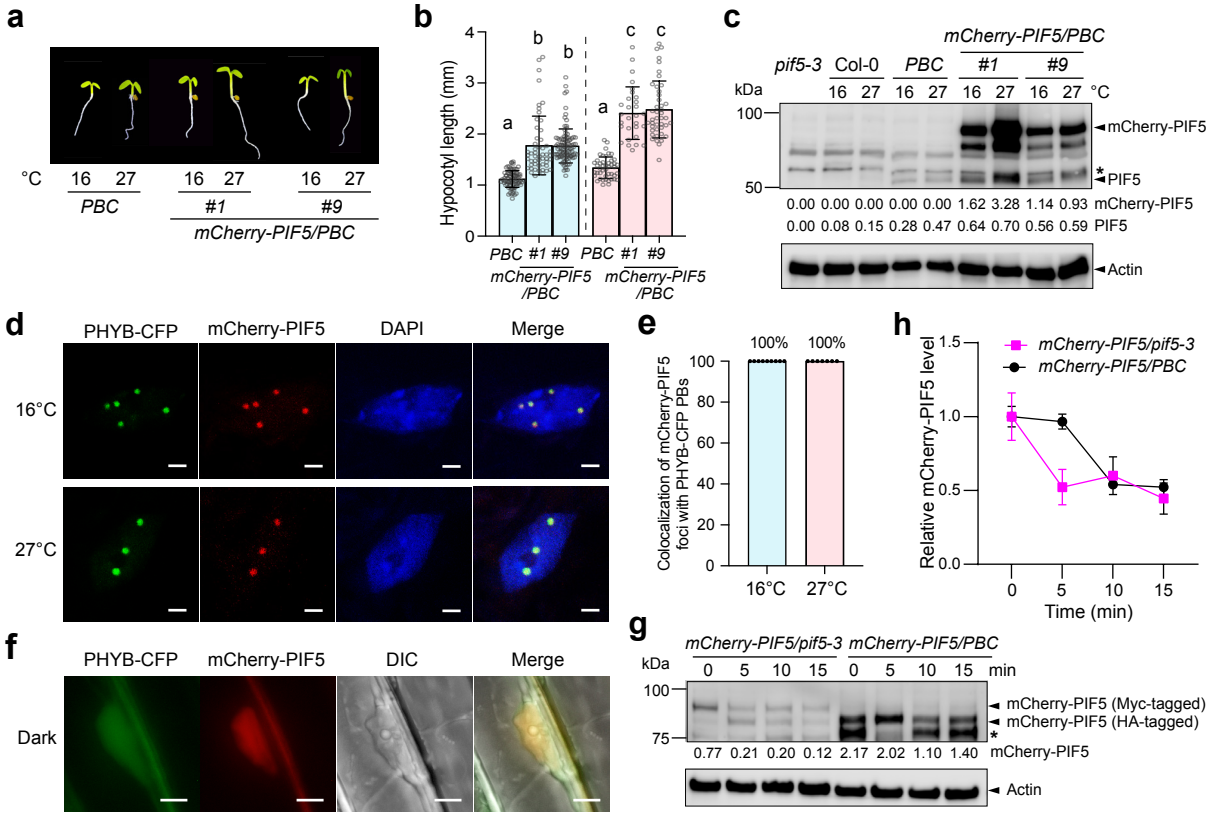

Fig. 4. PHYB recruits and stabilizes PIF5 in PBs. a Images of 4-d-old *PBC* and *mCherry-PIF5/PBC* (*#1* and *#9*) seedlings grown under 10 μmol m^{-2} s^{-1} R light at either 16°C or 27°C. **b** Hypocotyl length measurements of the seedings described in **a**. Error bars represent the s.d., and the center represents the mean (n ≥ 32 seedlings). Samples labeled with different letters exhibited statistically significant differences in hypocotyl length (ANOVA, Tukey's HSD, $p \leq 0.05$). **c** Immunoblots showing the steady-state levels of PIF5 or mCherry-PIF5 in 4-d-old *pif5-3*, Col-0, *PBC*, and *mCherry-PIF5* (*#1* and *#9*) seedlings grown under 10 μmol m^{-2} s^{-1} R light at either 16°C or 27°C. PIF5 and mCherry-PIF5 were detected by anti-PIF5 antibodies. Actin was used as a loading control. The asterisk indicates a non-specific band. The relative levels of PIF5 and mCherry-PIF5, normalized to the corresponding levels of actin, are shown below each lane. **d** Confocal images showing the colocalization of mCherry-PIF5 with PHYB-CFP in PBs in cotyledon pavement cells from 4-d-old *mCherry-PIF5/PBC #9* seedlings grown under 10 μmol m^{-2} s^{-1} R light at either 16°C or 27°C. Scale bars are equal to 2 μm. **e** Quantification of the colocalization of mCherry-PIF5 foci with PHYB-CFP PBs in the experiments as described in **d**. Error bars represent the s.e. (n = 9 biological replicates for the 16°C samples, n = 7 biological replicates for the 27°C samples), and the center represents the mean. **f** Fluorescence microscope images showing the localization of PHYB-CFP and mCherry-PIF5 in hypocotyl epidermal cells from 4-d-old dark-grown *mCherry-PIF5/PBC #9* seedings. The DIC image shows the nucleus. Scale bars are equal to 5 μm. **g** Immunoblots showing the degradation kinetics of Myc-tagged mCherry-PIF5 in *mCherry-PIF5/pif5-3* and HA-tagged mCherry-PIF5 in *mCherry-PIF5/PBC*. 4-d-old seedlings of *mCherry-PIF5/pif5-3* and *mCherry-PIF5/PBC #9* were incubated with cycloheximide and collected at the indicated time points. Total proteins were extracted at the indicated times and subjected to immunoblotting analysis using anti-PIF5 antibodies. Actin was used as a loading control. The asterisk indicates a nonspecific band. The relative mCherry-PIF5 levels normalized to the corresponding levels of actin are shown. **h**. Quantification of the relative mCherry-PIF5 levels shown in **g**. Error bars represent the s.d. of three independent replicates.

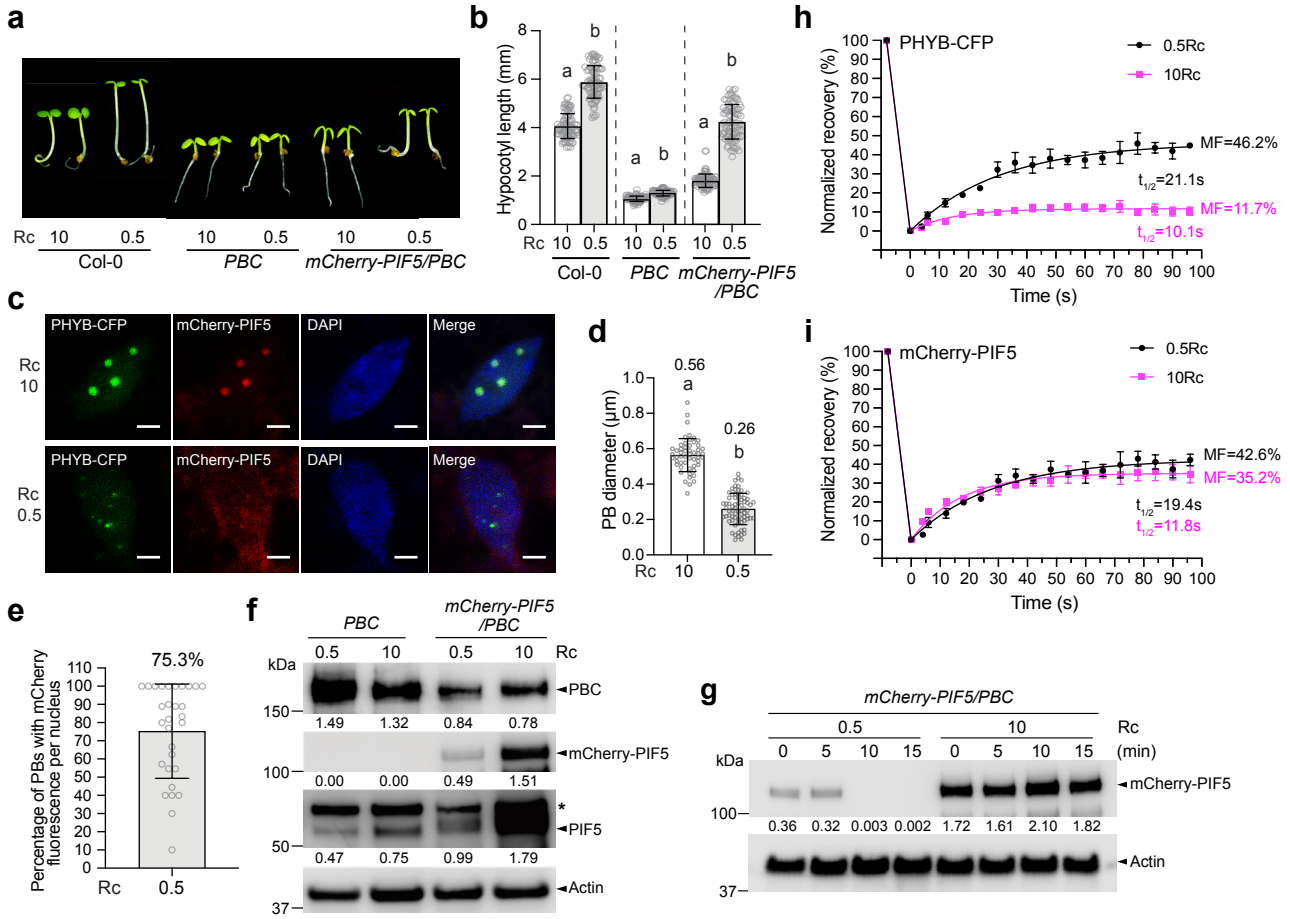

Fig. 5. Reducing PB size accelerates PIF5 degradation. a Images of 4-d-old Col-0, *PBC* and *mCherry-PIF5/PBC #9* seedlings grown under either 10 μmol m^{-2} s^{-1} or 0.5 μmol m^{-2} s^{-1} R light. **b** Hypocotyl length measurement of the seedlings described in **a**. Error bars represent the s.d., and the center represents the mean (n = 90 seedlings). Samples labeled with different letters exhibited statistically significant differences in hypocotyl length (Student's t-test, $p \leq 0.05$) **c** Confocal images showing of the PB patterns in cotyledon pavement epidermal cells from the *mCherry-PIF5/PBC* seedlings described in **a**. Scale bars are equal to 2 μm. **d** Quantification of the sizes of the PBs described in **c**. Error bars represent the s.d. and the center represents the mean (n = 53 PBs for the 10 μmol m^{-2} s^{-1} samples, n = 72 for the 0.5 μmol m^{-2} s^{-1} samples). Different letters denote statistically significant differences in PB size (Student's t-test, $p \leq 0.05$) **e** Quantification of the percentage PHYB-CFP PBs with detectable mCherry-PIF5 fluorescence in *mCherry-PIF5/PBC* seedlings grown under 0.5 μmol m^{-2} s^{-1} R light. Error bar represents the s.d., and the center represents the mean (n = 30). **f** Immunoblots of PHYB-CFP, endogenous PIF5 and mCherry-PIF5 in 4-d-old *PBC* and *mCherry-PIF5/PBC #9* seedlings grown under either 10 μmol m^{-2} s^{-1} or 0.5 μmol m^{-2} s^{-1} R light. Actin was used as control. The relative levels of PHYB-CFP, endogenous PIF5 and mCherry-PIF5, normalized to the corresponding actin levels, are shown under each lane. The asterisk indicates a non-specific band. **g** Immunoblots showing the degradation kinetics of mCherry-PIF5 in 4-d-old *mCherry-PIF5/PBC #9* seedlings grown under either 10 μmol m^{-2} s^{-1} or 0.5 μmol m^{-2} s^{-1} R light. Seedlings were incubated with cycloheximide and collected at the indicated time points. Total proteins were extracted at the indicated times and subjected to immunoblotting analysis using anti-PIF5 antibodies. Actin was used as a loading control. The relative mCherry-PIF5 levels normalized to the corresponding levels of actin are shown. **h** Results of FRAP experiments showing normalized fluorescence recovery plotted over time for PHYB-CFP in the *mCherry-PIF5/PBC #9* seedlings described in **a**. **i** FRAP experiments showing normalized fluorescence recovery plotted over time of mCherry-PIF5 in *mCherry-PIF5/PBC #9* seedlings described in **a**. For **h** and **i**, values represent the mean, and error bars represent the s.e. of at least three biological replicates. Solid lines represent exponential fit of the data. MF: mobile fraction; $t_{1/2}$ represents the half-time of fluorescence recovery.

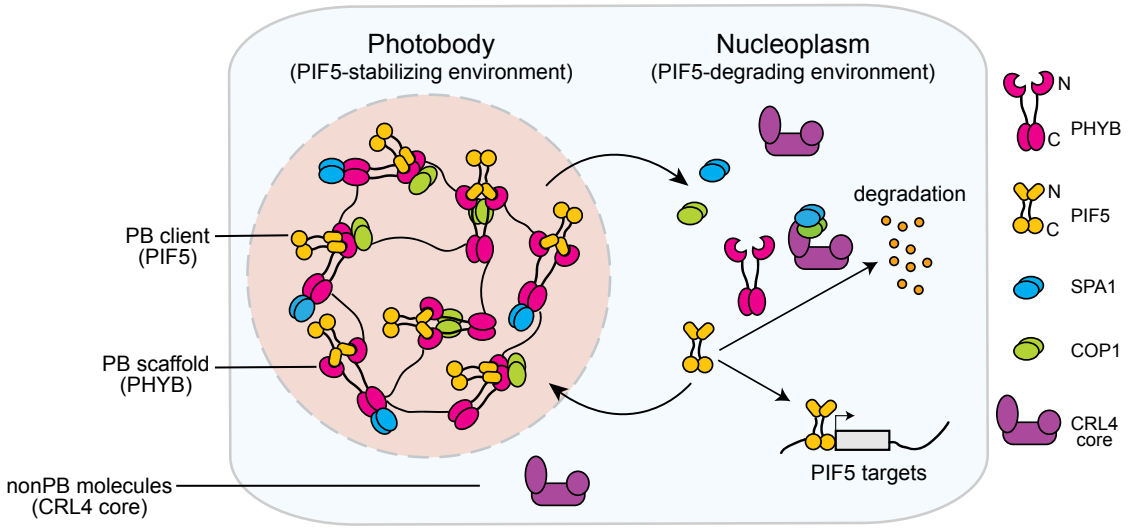

Fig. 6. A PB-enabled counterbalancing model for titrating nucleoplasmic PIF5. The condensation of PHYB creates a PIF5-stabilizing environment in PBs to counteract PIF5 degradation in the surrounding nucleoplasm. In the nucleoplasm, PHYB promotes PIF5 degradation by triggering its phosphorylation and ubiquitylation by the CRL4$^{COP1/SPA}$ E3 ubiquitin ligase[43,44,55]. In contrast, PBs stabilize PIF5 because only COP1 and SPAs, but not the CRL4 core, are localized to PBs[25,59,70], and the high concentration of PHYB in PBs disrupts the COP1-SPA complex via distinct interactions of COP1 with PHYB's N-terminal photosensory module and SPAs with PHYB's C-terminal output module[49–51,68,69]. PHYB serves as a scaffold component providing binding sites to recruit PIF5 as a client via direct interaction. Changes in light and temperature directly control the amount of active PHYB and thus the size of PBs to regulate the PB-to-nucleoplasmic partitioning of PIF5 and other PB constituents, thereby enabling an environmentally sensitive counterbalancing system to titrate nucleoplasmic PIF5 and its transcriptional output.